

# Nuclear receptor signaling regulates compartmentalized phosphatidylcholine remodeling to facilitate thermosensitive lipid droplet fusion

Received: 30 May 2024

Qi Li , Xiaofang Zhou, Xiaocong Zhang, Chuqi Zhang & Shaobing O. Zhang  

Accepted: 14 April 2025

Published online: 27 April 2025

 Check for updates

Lipid droplet (LD) fusion plays a key role in cellular fat storage. How the phospholipid monolayer membrane of LD functions in fusion, however, is poorly understood. In *Caenorhabditis elegans*, loss of cytochrome P450 protein CYP-37A1 causes de-repression of nuclear receptor DAF-12, promoting thermosensitive LD fusion. Here, we report that in *cyp-37A1* mutants, DAF-12 up-regulates the transcription and LD localization of seven fatty acid desaturases (FAT-1 to FAT-7) and a lysophosphatidylcholine acyltransferase 3 (LPCAT3) homolog MBOA-6. LD-targeting of these enzymes increases phosphatidylcholine (PC) containing  $\omega$ -3 C20 polyunsaturated fatty acids, which are essential for thermosensitive fusion.  $\omega$ -3 C20-PC increase LD membrane fluidity, as does high ambient temperature. Lowering LD membrane fluidity by a chemical membrane rigidifier attenuates thermosensitive fusion; ectopic targeting of  $\omega$ 3 desaturase FAT-1 or MBOA-6 to LDs increases fusion kinetics and thermosensitivity. Furthermore, human LPCAT3 localizes to LDs, positively regulates LD size in human cells and facilitates thermosensitive fusion in *C. elegans*. These results demonstrate that DAF-12 signaling regulates compartmentalized membrane remodeling and fluidization to facilitate conserved thermosensitive LD fusion.

When humans encounter fluctuations of the ambient temperature, temperatures of peripheral organs such as subcutaneous adipose may change considerably by as much as nine degrees<sup>1</sup>. For the body core to remain homeothermic at 37 °C, humans and mammals make systemic physiological adjustments, which include a change of fat metabolism involving the inter-conversion between brown/beige adipocytes and white adipocytes. A morphologically salient intracellular process underlying the conversion is the fusion of fat-storing lipid droplets (LDs) from multilocular small ones into a unilocular supersized entity<sup>2</sup>. To fuse or not to fuse is not only a result but also a regulatory factor of fat metabolism: the unilocular LD in white adipocytes is conducive to maximal fat storage at thermoneutral temperatures; multilocular LDs in brown adipocytes, for their larger surface-to-volume ratios, are

more accessible to enzymes for fat hydrolysis and mobilization under cold challenge<sup>3–6</sup>.

So far, two modes of LD fusion have been discovered by studies that concern LD size expansion during lipogenesis. One mode was discovered in mammals. In this mode, phospholipid monolayer membranes of the two fusing LDs do not seem to fuse. The triglyceride (TAG) content of the smaller LD is slowly and asymmetrically transferred to the bigger LD. A cell death-inducing DFF45-like effector (Cide) protein complex channels TAG transfer. The role of LD membrane in this process is unknown. This mode may be called lipid transfer or atypical fusion in morphological terms<sup>4,7–9</sup>. Another mode was discovered in mammals, *Drosophila*, and budding yeast. In this mode, membranes of the two LDs directly fuse and TAG contents

rapidly coalesce. This fusion morphologically resembles the direct fusion between vesicles with phospholipid bilayered membrane, hence the name coalescence or typical fusion. Typical fusion can be enhanced by raising cellular phosphatidic acid (PA) levels through knocking out Seipin protein or by lowering cellular phosphatidylcholine (PC) levels through knocking down CTP:phosphocholine cytidyltransferase 1 (CCT1) of the Kennedy pathway of de novo PC synthesis<sup>3,10-13</sup>. It was speculated that, having a small polar head, PA is conical in shape so as to endow LD membrane with a spontaneous negative curvability, which the cylindrical shape of PC energetically disfavors. Negative curvability is thought to facilitate the formation of connecting membranes between LDs for typical fusion, although membrane curvability has not been measured in the study of typical fusion<sup>10,12,14</sup>. Other factors potentially affecting the properties of phospholipids include the fatty acyl tails, especially the quintessential C20 & C22 polyunsaturated fatty acids (PUFAs). Typically, these PUFAs are incorporated into phospholipids not through de novo pathways but through a remodeling pathway called the Lands cycle, the key to which are the MBOAT family lysoPC/lysoPE/lysoPI acyltransferases (LPCAT/LPEAT/LPIAT)<sup>15-19</sup>. Whether PUFAs of LD membrane phospholipids affect atypical or typical LD fusion is unknown. Whether the ambient temperature regulates the two fusion processes per se is unknown either. Moreover, because both modes of fusion and even LD growth (direct synthesis and loading of TAG into an existing LD) occur in the same cell during lipogenesis and TAG storage<sup>3,20,21</sup>, it is difficult to attribute LD size expansion to just one process.

The poikilothermic model animal *C. elegans* is uniquely amenable to addressing the above questions for two reasons. First, LDs were identified in *C. elegans*<sup>22,23</sup>, and a clean model of LD fusion was established through a saturated genetic screen for *drop* mutants with LD size expansion<sup>24,25</sup>. In the mutant model of *drop-1/cyp-37A1*, lipogenesis, TAG level, and LD size are not different from those in wild-type (WT) at the regular ambient temperature of 20 °C. However, LDs in intestine cells of *cyp-37A1* fuse rapidly upon a shift to the high temperature of 30 °C, resulting in the formation of supersized LDs with diameters longer than the WT limit of 3 μm or even close to 8 μm at larval stage L4. CYP-37A1 protein is a cytochrome P450 monooxygenase, which together with the P450 oxidoreductase DROP-8/EMB-8 synthesizes an unidentified lipophilic agent that suppresses fusion. The suppression is effected through nuclear receptor DROP-31/DAF-12, a homolog of human nuclear receptors VDR and LXR. When DAF-12 is lost in function, thermosensitive fusion of *cyp-37A1* and *emb-8* mutants does not happen. Similar to typical fusion, thermosensitive fusion is rapid and direct fusion of LD membranes. Different from typical fusion, however, no significant changes of cellular PC and PA levels were detected in *cyp-37A1* or *daf-12* mutants. Thermosensitive LD fusion is intimately associated with a better organismal survival at high temperatures<sup>25</sup>. CYP-37A1 is orthologous to CYP4V2, the dysfunction of which causes Bietti's crystalline dystrophy (BCD) of retinal pigment epithelium (RPE) in humans<sup>26</sup>. Transgenic expression of human CYP4V2 in *C. elegans* can repress thermosensitive fusion<sup>25</sup>, implying the conservation of thermosensitive LD fusion and its mechanism across metazoans. Second, *C. elegans* expresses seven C16, C18, and C20 fatty acid desaturases named FAT, including Δ6 desaturase FAT-3 (the gating enzyme of C20 PUFA synthesis) conserved across species, and Δ12 desaturase FAT-2 and ω3 desaturase FAT-1 that vertebrates lack. Together with two fatty acid elongases, the seven desaturases functionally relay to catalyze saturated fatty acids (SFAs) into C18 monounsaturated fatty acids (MUUFAs) and C18/C20 ω-3 and ω-6 PUFAs at relatively constant levels. Genetic mutation of *fat* genes combined with dietary supplementation permits precise manipulation of most of the PUFAs<sup>27-30</sup>, which is hardly possible in mammals. The *C. elegans* genome also encodes enzymes of the Kennedy pathway and the CDP-DAG pathway for de novo phospholipid synthesis<sup>31</sup>. Moreover, *C. elegans* encodes MBOA-3/4/6/7, which were

among the first functionally cloned MBOA(T) family of LPLATs that remodel phospholipids with C20 PUFAs<sup>32,33</sup>. The mutant model of *cyp-37A1* and *daf-12* and the versatile genetic tools for manipulating fatty acids and phospholipids are poised to address the role of LD membrane in thermosensitive fusion.

We performed a large-scale forward genetic screen to have isolated and cloned about 30 new *drop* genes. These *drop* genes either suppress or enhance the thermosensitive LD fusion phenotype of *cyp-37A1* mutants. In this study, we report two suppressor genes *drop-33* and *drop-35* as encoding MBOA-6 and FAT-3. We then used systematic gene knockout to have examined the roles of FAT and MBOA(T) family proteins in thermosensitive LD fusion. Imaging and lipidomics showed that DAF-12 up-regulates the transcription and LD targeting of most of the FAT desaturases and MBOA-6/LPCAT3 to increase the level of ω-3 C20 PUFA-containing phospholipids and the fluidity of LD membrane. Evidence was obtained to show that the coordinated LD targeting of these enzymes and an increased fluidity of LD membrane are pivotal to thermosensitive fusion. A similar function of human LPCAT3 in LD size regulation and fusion was demonstrated.

## Results

### CYP-37A1 and DAF-12 regulate ω-3 C20 PUPA levels and the transcription of fatty acid desaturase genes

In *C. elegans*, mutation of *cyp-37A1* causes thermosensitive LD fusion, and mutation of *daf-12* abolishes it<sup>25</sup>. To begin to understand fusion mechanism, we used gas chromatography (GC) to measure total fatty acid compositions of these fusion mutants. The results showed that the mass percentages of ω-6 C20:4n6 and ω-3 C20:5n3 increase in *cyp-37A1* mutants and decrease to WT level when *daf-12* is also mutated (values in WT, *cyp-37A1*, and *cyp-37A1; daf-12* are  $1.30 \pm 0.03\%$ ,  $1.55 \pm 0.02\%$ , and  $1.21 \pm 0.02\%$  for C20:4n6, and,  $13.03 \pm 0.07\%$ ,  $13.79 \pm 0.13\%$  and  $11.84 \pm 0.08\%$  for C20:5n3). C20:3n6 and C20:4n3, the other two major C20 PUFAs, show no such changes (Fig. 1a). This led to the mass percentage of total C20 PUFAs increased from  $23.01 \pm 0.16\%$  in WT to  $24.02 \pm 0.23\%$  in *cyp-37A1*, and decreased to  $21.74 \pm 0.28\%$  when *daf-12* is also mutated (Fig. 1b). The total MUUFAs (C16:1n7, C18:1n9, and C18:1n7) show a similar pattern to C20 PUFAs ( $26.85 \pm 0.31\%$ ,  $28.29 \pm 0.18\%$ ,  $19.10 \pm 0.20\%$ ). Accordingly, C20 PUFA precursor C18 PUFA (C18:2n6) shows an opposite pattern of change ( $5.19 \pm 0.18\%$ ,  $4.22 \pm 0.02\%$ ,  $5.68 \pm 0.36\%$ ). The combined levels of SFAs and cyclic fatty acids (cyclo) also show an opposite pattern ( $41.83 \pm 0.28\%$ ,  $40.48 \pm 0.18\%$ ,  $50.67 \pm 0.14\%$ ) (Fig. 1a, b; Fig. S1a-c). These changes correlate or anti-correlate with fusion abilities of the mutants.

*C. elegans* synthesizes most of its MUUFAs and PUFAs de novo, using the seven desaturases FAT-1 to FAT-7<sup>30</sup>. Together with two elongases ELO-1 and ELO-2, these desaturases catalyze SFAs to MUUFAs and PUFAs in a stereotyped pathway (Fig. 1c). We conducted qRT-PCR to test whether mRNA levels of these *fat* genes change in *cyp-37A1* and *daf-12* mutants. Among the seven *fat* genes, *fat-1, 2, 3, 5*, and *7* increase in *cyp-37A1* and decrease to WT level in *cyp-37A1; daf-12*. The  $\Delta 9$  desaturase genes *fat-5* and *fat-7* increase the most in *cyp-37A1*, by  $4.35 \pm 0.10$  and  $4.08 \pm 0.22$  fold, respectively (Fig. 1d). The changes correlate with fusion capabilities and C20 PUFA levels. We then constructed transgenic lines expressing GFP reporter driven by *fat-5* promoter (*ssdSi5O*) and by *fat-7* promoter (*ssdSi52*). The promoter activities of *fat-5* and *fat-7* markedly increase in *cyp-37A1*, by  $1.77 \pm 0.13$  and  $2.04 \pm 0.13$  fold, respectively. The activities decrease back to or below WT levels in *cyp-37A1; daf-12* (Fig. S2a-c). These results show that CYP-37A1 and DAF-12 regulate in an opposite manner the transcription of *fat-5* and *fat-7* and to a lesser extent the transcription of *fat-1, fat-2*, and *fat-3*. In contrast, mRNA levels of the negative control gene *tbb-2* and of the elongase genes *elo-1, elo-2*, and *elo-5* are not such regulated (Fig. S2d). We used a constitutive promoter *vha-6p* to express FLAG::GFP::FAT fusion proteins in WT, *cyp-37A1*, and *cyp-37A1; daf-12*. The results showed that CYP-37A1 and DAF-12 do not regulate the

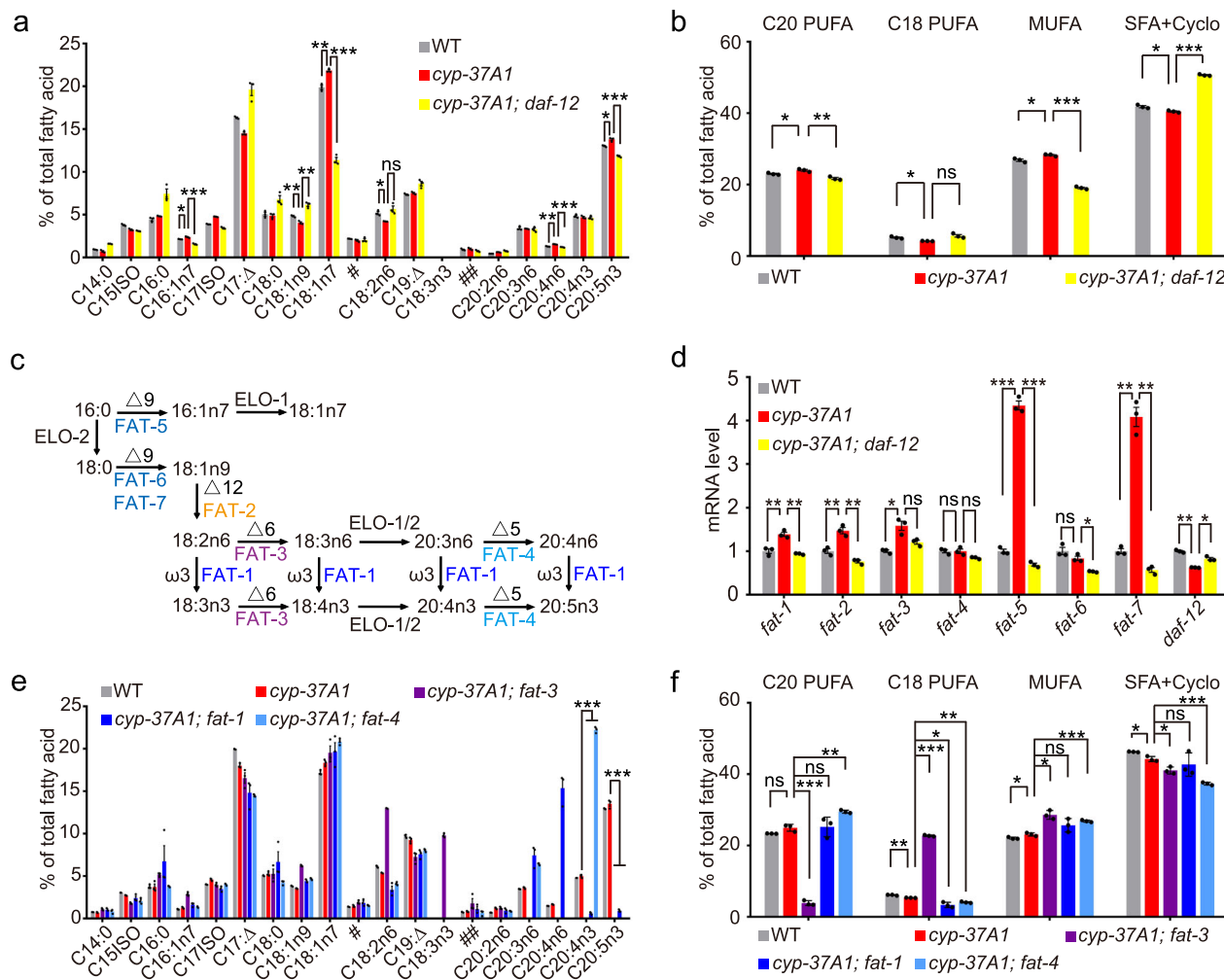


**Fig. 1 | Fatty acid compositions and gene expression levels in *cyp-37A1*, *daf-12*, and *fat* mutants.** **a, b** Total fatty acid compositions of WT, *cyp-37A1(ssd9)*, and *cyp-37A1(ssd9); daf-12(m583)* mutants. The identities of all fatty acids except two unknown ones (# and ##) are indicated. The level is plotted as a mass percentage. The levels of C20 PUFAs, C18 PUFAs, MUFA, and SFAs plus cyclic fatty acids (cyclo) are plotted in **(b)**. Data are mean  $\pm$  SEM.  $N = 3$  biological replicates. Value of each replicate is shown as a dot (the same applies to other column graphs with  $N \leq 6$  if not otherwise indicated). Gas chromatography (GC) experiments with L4 stage animals. **c** The synthesis of MUFA and PUFAs in *C. elegans*. The seven fatty acid desaturases (FAT-1 to FAT-7), the positions of double bonds introduced, and cognate substrates and products are denoted. Also denoted are the elongases ELO-1 and ELO-2 and the reactions they catalyze. **d** mRNA levels of *fat* and *daf-12* genes in WT, *cyp-37A1*, and *cyp-37A1; daf-12* mutants. Data are mean  $\pm$  SEM.  $N = 3$  biological replicates. qRT-PCR experiments with L4 stage animals. **e, f** Total fatty acid compositions of WT, *cyp-37A1(ssd9)*, *cyp-37A1(ssd9); fat-3(ok1126)*, *cyp-37A1(ssd9); fat-1(ok2323)*, and *cyp-37A1(ssd9); fat-4(ok958)* mutants. The levels of C20 PUFAs, C18 PUFAs, MUFA, and SFAs+Cyclo are plotted in **(f)**. Data are mean  $\pm$  SEM.  $N = 3$  biological replicates. GC experiments with L4 stage animals. For all statistical analyses, non-significant (ns) is  $P \geq 0.05$ . \*,  $P < 0.05$ . \*\*,  $P < 0.01$ . \*\*\*,  $P < 0.001$ . Unpaired two-sample two-tailed *t*-test. All exact *P*-values and source data of **(a, b, d–f)** are provided as Source Data file.

and ELO-2 and the reactions they catalyze. **d** mRNA levels of *fat* and *daf-12* genes in WT, *cyp-37A1*, and *cyp-37A1; daf-12* mutants. Data are mean  $\pm$  SEM.  $N = 3$  biological replicates. qRT-PCR experiments with L4 stage animals. **e, f** Total fatty acid compositions of WT, *cyp-37A1(ssd9)*, *cyp-37A1(ssd9); fat-3(ok1126)*, *cyp-37A1(ssd9); fat-1(ok2323)*, and *cyp-37A1(ssd9); fat-4(ok958)* mutants. The levels of C20 PUFAs, C18 PUFAs, MUFA, and SFAs+Cyclo are plotted in **(f)**. Data are mean  $\pm$  SEM.  $N = 3$  biological replicates. GC experiments with L4 stage animals. For all statistical analyses, non-significant (ns) is  $P \geq 0.05$ . \*,  $P < 0.05$ . \*\*,  $P < 0.01$ . \*\*\*,  $P < 0.001$ . Unpaired two-sample two-tailed *t*-test. All exact *P*-values and source data of **(a, b, d–f)** are provided as Source Data file.

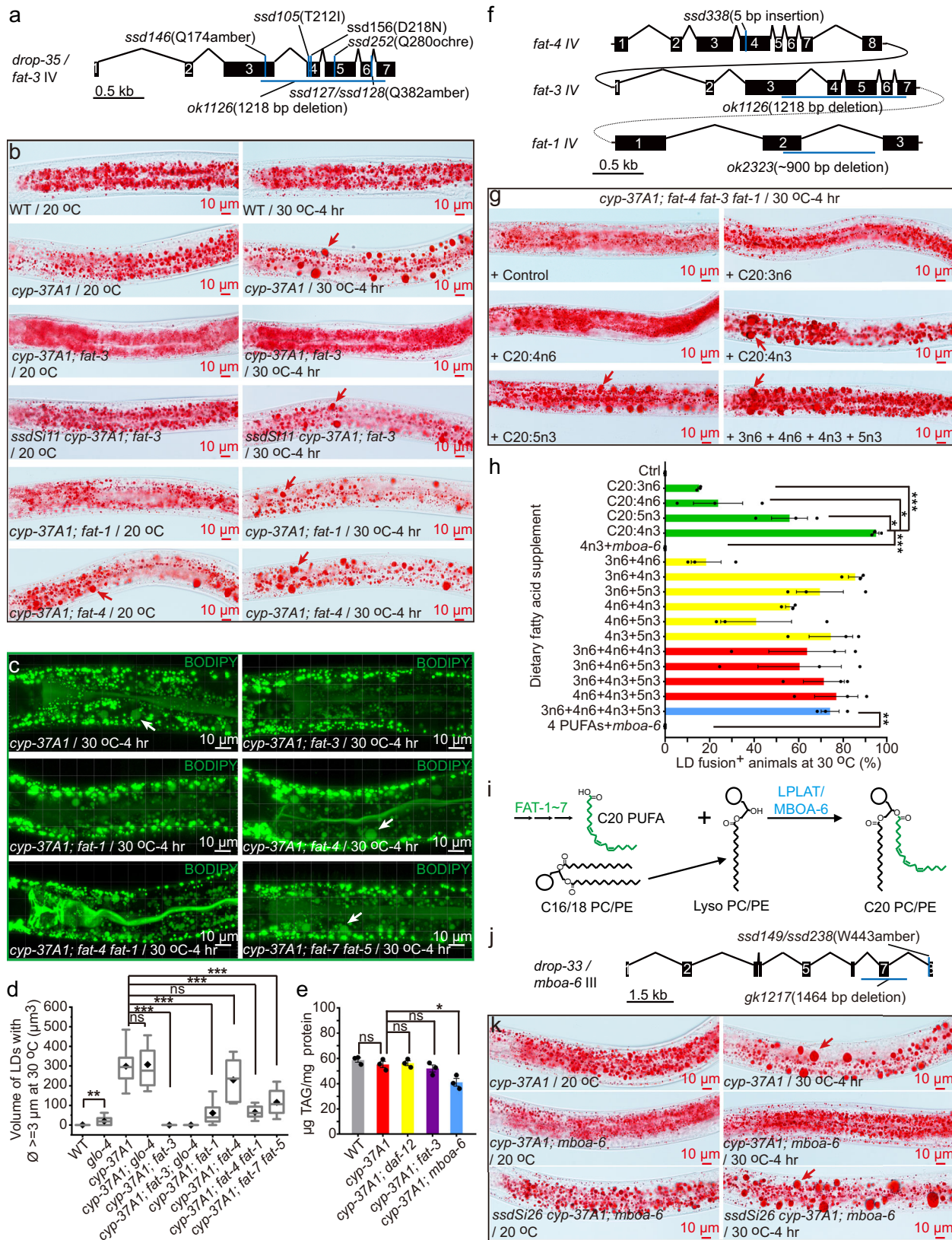
translation or the stability of FAT proteins or an LD marker protein DGAT-2 (Fig. S2e).

Since C20 PUFA levels correlate with fusion abilities, we used GC to measure fatty acid compositions of *cyp-37A1* mutant in double with deletion mutant of *fat-3*, *fat-1*, or *fat-4* (Fig. S1d-f). In *cyp-37A1; fat-3*, very little C20 PUFAs are synthesized ( $3.90 \pm 0.40\%$  vs.  $25.00 \pm 0.56\%$  in *cyp-37A1*), and their precursors C18 PUFAs accumulate accordingly ( $22.76 \pm 0.11\%$  vs.  $5.36 \pm 0.03\%$ ). In *cyp-37A1; fat-1*,  $\omega_3$  C20:4n3 and C20:5n3 disappear and precursors  $\omega_6$  C20:3n6 and C20:4n6 increase, with the total C20 PUFA level unchanged ( $25.24 \pm 1.58\%$  vs.  $25.00 \pm 0.56\%$ ). In *cyp-37A1; fat-4*, C20:4n6 and C20:5n3 disappear, and precursors C20:3n6 and especially C20:4n3 increase ( $22.32 \pm 0.18\%$  vs.  $5.00 \pm 0.12\%$ ), with the total C20 PUFA level increased ( $29.51 \pm 0.24\%$  vs.  $25.00 \pm 0.56\%$ ) (Fig. 1e, f). In another experiment, we measured fatty acid compositions of WT, *fat-3*, *fat-1*, and *fat-4* single mutants. The C20 PUFA levels in WT and *fat* mutants are  $19.16 \pm 0.50\%$ ,  $1.26 \pm 0.08\%$ ,  $23.56 \pm 0.71\%$ , and  $22.94 \pm 0.90\%$ , respectively (Fig. S1l, m). The pattern

of change is similar to that in *cyp-37A1* background (Fig. 1f). These results show that the synthesis of C20 PUFAs relies absolutely on FAT-3/1/4, and CYP-37A1 and DAF-12 fine-tune the synthesis through transcriptional regulation. The *fat* mutants should allow testing the effects of C20 PUFAs on thermosensitive fusion of *cyp-37A1*.

#### FAT desaturases for $\omega_3$ C20 PUFA synthesis and the MBOA-6/LPCAT3 enzyme for phospholipid remodeling are specifically required for thermosensitive LD fusion

In the *cyp-37A1* suppressor screen, we have isolated and cloned many new *drop* genes that when mutated suppress the fusion phenotype. One of these genes was reported as *drop-31/daf-12*<sup>25</sup>. We now report the cloning of *drop-35* as *fat-3* mutation (Fig. 2a). The six cloned nonsense and missense *fat-3* alleles and an independent deletion allele *ok1126* completely suppress the thermosensitive fusion phenotype of *cyp-37A1*; no supersized LDs (diameter  $\geq 3 \mu\text{m}$ ) form at  $30^\circ\text{C}$  as shown qualitatively by postfix Oil Red O staining and imaging (Fig. 2b). The



phenotype was verified quantitatively by vital green BODIPY labeling/imaging and measuring volumes of supersized LDs in the two cells of the second intestine segment, and, by counting the percentage of fusion-positive animals (Fig. 2c, d; Table S1). The volumes of supersized LDs in WT, *cyp-37A1*, and *cyp-37A1; fat-3* are  $0.94 \pm 0.94 \mu\text{m}^3$ ,  $298.44 \pm 36.61 \mu\text{m}^3$ , and  $0.00 \pm 0.00 \mu\text{m}^3$ , respectively. For measuring

volumes of supersized LDs, eliminating lysosome-related organelles (LROs) by *glo-4* mutation makes no difference: the volumes of *glo-4*, *cyp-37A1; glo-4*, and *cyp-37A1; fat-3; glo-4* are  $20.14 \pm 5.27 \mu\text{m}^3$ ,  $306.83 \pm 32.39 \mu\text{m}^3$ ,  $0.00 \pm 0.00 \mu\text{m}^3$ , almost the same as those without *glo-4* (Fig. 2d). *fat-3* mutation seems to bring down LD sizes further to be much smaller than WT (Fig. 2b). Transgenic expression of

**Fig. 2 | Effects of C20 PUFAs and phospholipid fatty acyl tail remodeling on thermosensitive LD fusion.** **a** The *cyp-37A1* suppressor mutant *drop-33* is mutated in *fat-3*. All mutant alleles except *ok1126* are from this study. **b** LD fusion phenotypes of WT, *cyp-37A1*, *cyp-37A1; fat-3*, *cyp-37A1; fat-3* rescued by the transgenic line *ssdSi11/vha-6p::fat-3::3xflag::gfp*, *cyp-37A1; fat-1*, and *cyp-37A1; fat-4*. Oil Red O staining. Note the formation of supersized LDs (diameter  $\geq 3 \mu\text{m}$ , arrows) upon shift to 30 °C for 4 h as a result of thermosensitive fusion. **c, d** LD fusion phenotypes of *cyp-37A1*, *cyp-37A1; fat-3*, *cyp-37A1; fat-1*, *cyp-37A1; fat-4*, *cyp-37A1; fat-4 fat-1*, and *cyp-37A1; fat-7(wa36) fat-5(tm420)*. C1-BODIPY 500/510-C12 vital staining and confocal imaging. The total volume of supersized LDs (arrows) in the second intestine segment of each animal was measured and presented (**d**).  $N = 19, 18, 13, 20, 10, 18, 16, 11, 13$ , and 18 animals, respectively. Data are presented as box-whisker plot, which shows the lower extreme (10%), lower quartile, median, upper quartile, upper extreme (90%), and mean (diamond) values. **e** TAG levels of WT, *cyp-37A1*, *cyp-37A1*;

*daf-12*, *cyp-37A1; fat-3*, and *cyp-37A1(ssd9); mboa-6(ssd238)*.  $N = 3$  biological replicates. **f** Configuration of linked triple mutant *fat-4(ssd338) fat-3(ok1126) fat-1(ok2323)*. **g, h** LD phenotypes and fusion-positive percentages of *cyp-37A1; fat-4 fat-1* animals supplemented with dietary C20 PUFAs each at a final concentration of 0.33 mM. Arrows point to supersized LDs. For each data point, more than fifty L4 stage animals from a replicate plate were counted, and percentage values of three replicates were averaged. **i** Incorporation of C20 PUFAs into PC and PE through phospholipid remodeling. **j** The *cyp-37A1* suppressor mutant *drop-33* is mutated in *mboa-6*. Alleles *ssd149* and *ssd238* are from this study. **k** LD fusion phenotypes of *cyp-37A1*, *cyp-37A1; mboa-6*, and *cyp-37A1; mboa-6* rescued by *ssdSi26/vha-6p::mboa-6::3xflag::gfp*. Oil Red O staining. Arrows point to supersized LDs. For (**e, h**), data are mean  $\pm$  SEM. For statistical tests, ns is  $P \geq 0.05$ . \* $P < 0.05$ . \*\* $P < 0.01$ . \*\*\* $P < 0.001$ . Unpaired two-sample two-tailed *t*-test. All exact *P*-values and source data of (**d, e, h**) are provided as Source Data file.

FAT-3::FLAG::GFP fusion protein in intestine cells (*ssdSi11*) completely restores the fusion phenotype in *cyp-37A1; fat-3* mutant (Fig. 2b; Table S1). The *cyp-37A1* mutant is a model of LD size enlargement, specifically by fusion, with no contribution from LD growth or hydrolysis so that the TAG level is not altered<sup>25</sup>. Suppressor mutants *daf-12* and *fat-3* do not alter the TAG level of *cyp-37A1* either ( $56.12 \pm 1.90$ ,  $51.95 \pm 2.74$  vs.  $55.12 \pm 2.48 \mu\text{g}/\text{mg}$  protein) (Fig. 2e). Moreover, there are neither detectable C20 PUFAs in TAG nor changes of TAG fatty acid composition in WT and the fusion mutants (Fig. S1g-k). It indicates a specific role of C20 PUFAs in fusion that does not involve TAG synthesis or hydrolysis.

The functions of  $\omega$ -3 and  $\omega$ -6 C20 PUFAs may be separately tested by using *fat-1* and *fat-4* mutants (Fig. 1e). We surprisingly found that *fat-1* mutation significantly suppresses thermosensitive fusion while *fat-4* hardly does so: supersized LD volumes of *cyp-37A1; fat-1* and *cyp-37A1; fat-4* are  $61.28 \pm 14.98 \mu\text{m}^3$  and  $229.90 \pm 33.32 \mu\text{m}^3$ , respectively. *fat-4* increases the thermosensitivity of fusion instead: 29.2% *cyp-37A1; fat-4* animals already fuse LDs at 20 °C and 100% at 30 °C, while 0% *cyp-37A1; fat-1* animals fuse at 20 °C and 81.3% at 30 °C (Fig. 2b-d; Table S1). C16 and C18  $\Delta$ 9 desaturases FAT-5/6/7 and  $\Delta$ 12 desaturase FAT-2 function sequentially to synthesize C18:2n6, a key precursor of C20 PUFAs. Single and double mutants of *fat-5/6/7/2* suppress thermosensitive fusion to various extent, with *fat-6; fat-7* double mutant (gating C18:1n9) and *fat-2* single mutant (gating C18:2n6) being most potent (Fig. 2c, d; Table S1). However, *fat-6; fat-7*, and *fat-2* have additional defects and are very sick. These data, together with the result that C20:4n3 accumulates significantly in *cyp-37A1; fat-4*, indicate that  $\omega$ -3 C20 PUFAs and particularly C20:4n3 are more potent than  $\omega$ -6 C20 PUFAs in supporting thermosensitive fusion.

To further test the potency of each of the four major C20 PUFAs, we created a triple deletion mutant of *fat-4/3/1* by CRISPR and homologous recombination (Fig. 2f). The triple mutant was introduced into *cyp-37A1*, in which each diet-supplemented C20 PUFA would no longer be converted to other PUFAs. The four C20 PUFAs (0.33 mM in the agar medium) restore thermosensitive fusion phenotype of *cyp-37A1; fat-4 fat-3 fat-1* to various degrees. In terms of percentage of fusion-positives, C20:4n3 is the most potent, restoring  $94.79 \pm 1.28\%$  compared to  $55.91 \pm 8.07\%$  by C20:5n3,  $15.34 \pm 0.53\%$  by C20:3n6, and  $23.81 \pm 11.07\%$  by C20:4n6 (Fig. 2g, h). Supplementation of any other C20 PUFA with C20:4n3 does not further increase but decrease the percentage of positives (Fig. 2h). It suggests that the concentration of each PUFA has reached saturation, and C20 PUFAs compete with each other for a shared pathway to regulate fusion.

Since almost no C20 PUFA is incorporated into TAG (Fig. S1g-k), the shared pathway is likely via being trans-acylated to lysophospholipids to form remodeled phospholipids, i.e., the Lands cycle (Fig. 2i). Key to Lands cycle is the MBOAT family acyltransferases, of which *C. elegans* encodes nine. The main one, MBOA-6 (homolog of human LPCAT3), trans-acylates PUFAs to remodel PC, PE, and PS<sup>33</sup>.

MBOA-7 (LPIAT1) remodels PI<sup>32</sup>. MBOA-3 and MBOA-4 (LPCAT4 and LPEAT1) probably remodel PE and PS. MBOA-1 (SOAT1 and SOAT2) and MBOA-2 (DGAT1) likely function in neutral lipid synthesis. The other three are HHAT-1, HHAT-2, and MOM-1, human homologs of which trans-acylate proteins<sup>19</sup> (Fig. S3a).

Interestingly, another *cyp-37A1* suppressor gene *drop-33* is mutated in MBOA-6/LPCAT3 (Fig. 2j). Two nonsense alleles *ssd149* and *ssd238* are mutated in the same site and completely suppress thermosensitive fusion of *cyp-37A1* to 0% (Fig. 2k; Table S1). *mboa-6* mutation slightly reduces the TAG level of *cyp-37A1* ( $41.14 \pm 3.10$  vs.  $55.12 \pm 2.48 \mu\text{g}/\text{mg}$  protein) (Fig. 2e). A deletion allele *gk1217* also completely suppresses thermosensitive fusion but its homozygotes are lethal, suggesting that the viable alleles *ssd149* and *ssd238* are partial loss-of-function. Thermosensitive fusion can be restored by transgenic expression of MBOA-6::FLAG::GFP fusion protein (*ssdSi26*) in intestine cells of *cyp-37A1; mboa-6* (Fig. 2k; Table S1). We obtained and created by CRISPR deletion alleles of the other five *mboa* genes (Fig. S3b). *mboa-3* and *mboa-7* mutations suppress fusion-positive *cyp-37A1* mutants down to 20.9% and 76.2%, respectively. *mboa-1* and *mboa-4* only slightly suppress, down to 89.6% and 95.2%. *mboa-2* does not suppress. *mboa-3*, *mboa-4*, and *mboa-7* display additive effects. However, even *mboa-3/4/7* triple mutation does not completely suppress thermosensitive fusion (Table S1). Thus, MBOA-6 is the main phospholipid remodeling enzyme required for thermosensitive fusion. *mboa-6* mutation also completely abolishes the fusion phenotype of *cyp-37A1; fat-4 fat-3 fat-1* supplemented with C20 PUFAs and the enhanced fusion phenotype of *cyp-37A1; fat-4* (Fig. 2h; Table S1). *C. elegans* PCYT-1 and CEPT-1 are orthologous to human CCT1 and CEPT1 of the Kennedy pathway of de novo PC synthesis<sup>31</sup>. However, mutations of *pcyt-1* and *cept-1* do not affect the percentage of fusion-positives (Table S1). It suggests that thermosensitive fusion is more sensitive to PC/PE/PS remodeled with C20 PUFAs than to PC/PE/PS synthesized de novo.

### CYP-37A1 and DAF-12 regulate the targeting of desaturases and MBOA-6 to LDs

mRNA levels of all nine MBOAT family genes do not show a pattern consistent with the fusion capabilities of *cyp-37A1* and *daf-12* mutants, however (Fig. S3c). Protein translation or stability of MBOA-6 shows no such a pattern either (Fig. S2e). Since the changes of C20 PUFAs in total fatty acids are small between WT, *cyp-37A1*, and *cyp-37A1; daf-12*, mechanism in addition to transcriptional regulation may be involved. We asked whether CYP-37A1 and DAF-12 regulate the subcellular localization of FAT desaturases and MBOA-6. Transgenic lines expressing FAT::FLAG or MBOA-6::FLAG fusion proteins by *vha-6* promoter were brought into fusion mutants. These lines also carry a *glo-4(ok623)* mutation, which eliminates LROs so that red BODIPY-558/568-C12 vital labels LDs specifically<sup>23</sup>. In vivo confocal imaging was then conducted to measure the distribution of GFP signal

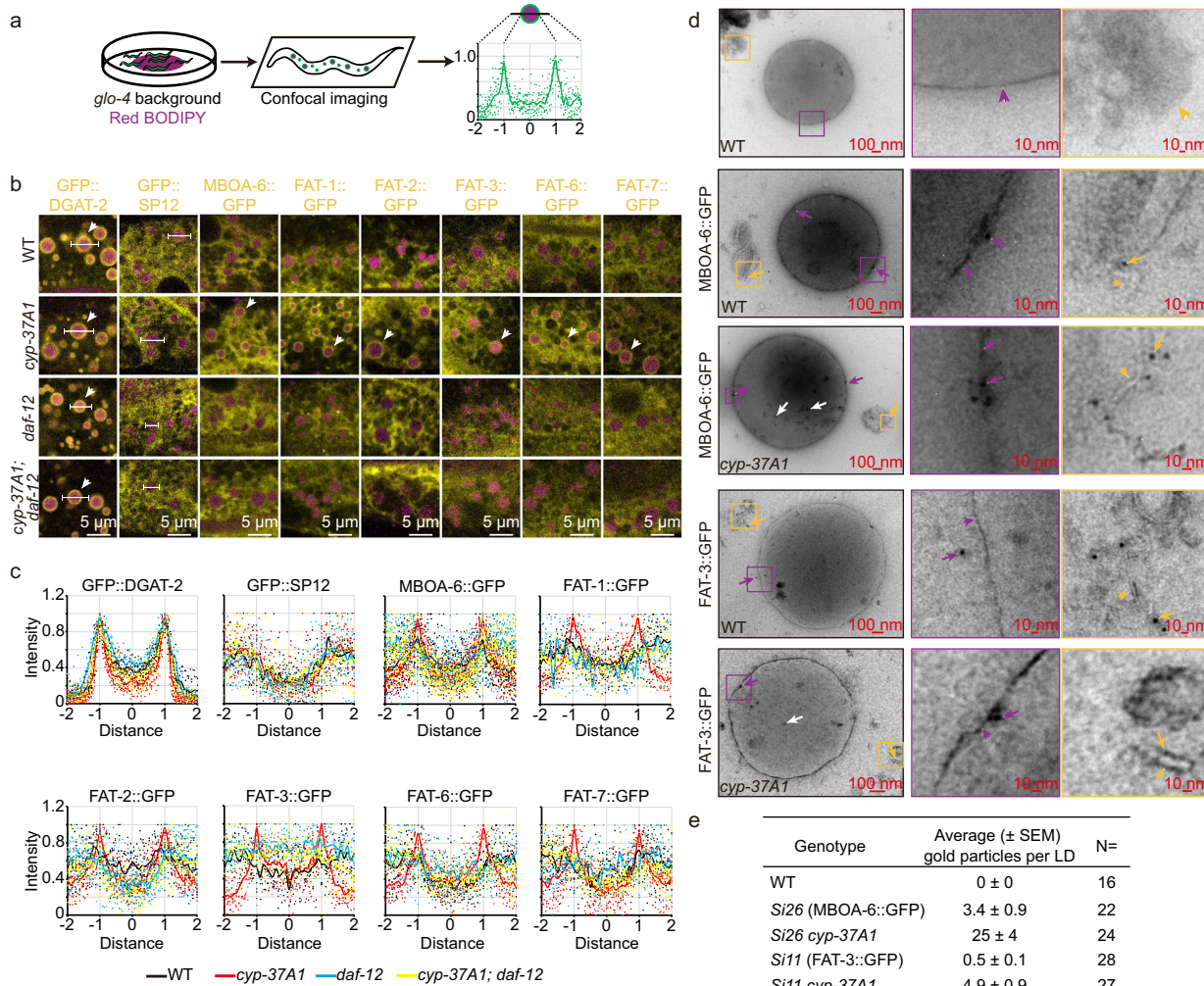


**Fig. 3 | Subcellular localization of desaturases and MBOA-6 in *cyp-37A1* and *daf-12* mutants.** **a** Flowchart of in vivo imaging and measuring the location of transgenic GFP fusion proteins relative to LDs. **b, c** Subcellular location of GFP fusion proteins in *cyp-37A1* and *daf-12* mutants. The fusion proteins were expressed in intestine cells driven by *uha-6* promoter in transgenic lines *hjSi56* (FLAG::GFP::D-GAT-2), *hjSi14* (GFP::SP12), *ssdSi32* (FAT-1::FLAG::GFP), *ssdSi33* (FAT-2::FLAG::GFP), *ssdSi11* (FAT-3::FLAG::GFP), *ssdSi24* (FAT-6::FLAG::GFP), *ssdSi25* (FAT-7::FLAG::GFP), and *ssdSi26* (MBOA-6::FLAG::GFP). LDs were labeled by red BODIPY (magenta). Arrowheads point to examples of localization to LD. Lines illustrate the line measurement tool. Each image is a single optical section of a confocal Z-stack of a typical animal.  $N \geq 10$  animals. The GFP intensity around a randomly picked LD was measured and plotted.  $N \geq 10$  LDs for each data line. **d** Immunogold labeling and TEM of LDs. Samples were LDs purified from the transgene-negative WT (the 1st row, negative control), LDs purified from WT and *cyp-37A1* expressing MBOA-

6::FLAG::GFP (*ssdSi26*) (the 2nd and 3rd row), and LDs purified from WT and *cyp-37A1* expressing FAT-3::FLAG::GFP (*ssdSiII*) (the 4th and 5th row). Magenta boxed area shows LD (zoom-in, middle panel). Yellow boxed area shows residual microsomal contaminations (zoom-in, right panel). Magenta arrows and arrowheads point to gold particles on monolayer membranes of LDs. Yellow arrows and arrowheads point to gold particles on bilayered membranes of microsomes. Gold particles were against the GFP epitope and 5 nm in size. Note: LD samples were whole mounted onto TEM grids, and LDs were thus flattened to some degree. The particles seen within the LD perimeter (white arrows) were not inside the LD but on the flattened LD membrane. **e** Average number of gold particles localized to an LD from each genotype. Gold particles within and no more than 10 nm outside of the LD perimeter were counted as being localized to the LD. Gold particles localized to microsomal membranes attached to LDs were not counted. Source data of (e) is provided as Source Data file.

in relation to LDs (Fig. 3a). The result showed that in WT, FLAG::GFP fusion proteins of MBOA-6 (*ssdSi26*), and of desaturases for PUFA synthesis, FAT-1 (*ssdSi32*), FAT-2 (*ssdSi33*), FAT-3 (*ssdSi11*), FAT-6 (*ssdSi24*), and FAT-7 (*ssdSi25*) all display a reticular pattern typical of endoplasmic reticulum (ER). However, in *cyp-37A1* these proteins closely encircle a large number of LDs. In *cyp-37A1; daf-12* the LD localization is diminished. The localization pattern correlates with fusion abilities. In contrast, the LD marker protein GFP::DGAT-2 (*hjSi56*) consistently localizes to LDs and the ER marker GFP::SP12 (*hjSi14*) always localizes to ER in WT and fusion mutants (Fig. 3b, c).

The LD localization of transgenic FAT and MBOA-6 proteins in fusion mutants is not all-or-none. To quantify the localization, from the above transgenic lines we purified LDs and microsomes (TM) using

density centrifugation and then conducted in vitro confocal imaging, western blot, and immunogold transmission electron microscopy (TEM) (Fig. S4a). To test whether the purification method we use yields LD samples with good purity, we did a pilot experiment to purify LDs and TMs from three transgenic lines expressing LD marker FLAG::GFP::DGAT-2 (*hjS156*), ER marker GFP::SP12 (*hjS14*), and peroxisome marker GFP::DAF-22 (*hjS173*). Equal masses of LD and TM proteins were loaded onto a dot blot membrane and into SDS-PAGE gels in parallel. Coomassie staining of the dot blot showed that equal masses of proteins were loaded. Western blot against these markers and endogenous mitochondrial marker protein ATP-1 showed that LD samples contain very little contamination from ER, peroxisome, or mitochondrion (Fig. S4b, c). Western blot and confocal imaging

verified that the control LD marker GFP::DGAT-2 and ER marker GFP::SP12 localize to purified LD and TM respectively, with little difference between in WT, *cyp-37A1*, and *cyp-37A1; daf-12*. In contrast, FAT-1::GFP, FAT-2::GFP, FAT-3::GFP, FAT-6::GFP, FAT-7::GFP, and MBOA-6::GFP localize to LD more in *cyp-37A1* than in WT and *cyp-37A1; daf-12* (Fig. S4d-f). This pattern of localization is consistent with that revealed by *in vivo* imaging. The five FAT proteins and MBOA-6 in TM show no such a pattern (Fig. S4d). LDs purified from FAT-3::GFP and MBOA-6::GFP transgenic lines were subjected to immunogold labeling of the GFP tag and TEM. The results showed that in the non-transgenic WT control, no gold particle is present. In the transgenic WT, few gold particles localize to LDs. In the transgenic *cyp-37A1*, in contrast, many more gold particles localize to LDs (Fig. 3d, e). In *cyp-37A1*, the majority of LD-localized gold particles localize directly to the LD monolayer membrane, and, few do localize to bilayer microsomal membranes attached to LD (Fig. 3d). These results demonstrate that CYP-37A1 and DAF-12 quantitatively regulate the targeting of FAT desaturases and MBOA-6 to LD membrane.

### CYP-37A1 and DAF-12 regulate C20 PUFA-PC/PE levels and LD membrane fluidity through desaturases and MBOA-6

The increased transcription and LD targeting of FAT desaturases and MBOA-6 in *cyp-37A1* mutants suggests that these enzymes may remodel phospholipids of LD membrane. Thus, we purified LDs for lipidomics analysis. In WT LDs, PC is  $76.49 \pm 1.51\%$  (molar percentage) of total LD phospholipids. PE, PI, and PS are  $7.58 \pm 0.73\%$ ,  $9.29 \pm 1.49\%$ , and  $4.60 \pm 0.76\%$ , respectively. Other phospholipids are of relatively low levels, less than 1%. PA is less than 0.1% (Fig. 4a). In *cyp-37A1* LD, levels of major phospholipid classes are not changed except that LPE is significantly increased, suggesting that its fusion ability is not due to changes of levels of major LD phospholipid classes. When the fusion suppressor mutant *daf-12; fat-3*, or *mbo-6* is introduced into *cyp-37A1*, PC is increased while PI, PS, PA, and LPE are reciprocally decreased (Fig. 4a).

Each class of phospholipid may be divided into subspecies. A subspecies is defined by the number of carbon atoms and the number of double bonds of two individual fatty acid tails. As revealed by lipidomics, PC subspecies containing C20 PUFAs such as PC(20:4/16:0) and PC(20:5/16:0) increase in *cyp-37A1* and decrease in *cyp-37A1; daf-12*, *cyp-37A1; fat-3*, and *cyp-37A1; mbo-6* (Fig. 4b). The molar percentages of PC(20:4/16:0) and PC(20:5/16:0) combined in total LD PL are  $1.07 \pm 0.16\%$  (WT),  $2.72 \pm 0.23\%$  (*cyp-37A1*),  $1.57 \pm 0.06\%$  (*cyp-37A1; daf-12*),  $0.07 \pm 0.01\%$  (*cyp-37A1; fat-3*), and  $0.52 \pm 0.07\%$  (*cyp-37A1; mbo-6*) and the increases and decreases show statistical significance (Fig. 4d). The four identified PC(20/20) subspecies combined and the six PC(20/18) subspecies combined show a similar pattern of change, although some changes are not significant (Fig. 4b, d). Similarly, molar percentages of PE subspecies PE(20:4/16:0) and PE(20:3/16:0) combined are  $0.17 \pm 0.02\%$  (WT),  $0.24 \pm 0.04\%$  (*cyp-37A1*),  $0.17 \pm 0.01\%$  (*cyp-37A1; daf-12*),  $0.02 \pm 0.00\%$  (*cyp-37A1; fat-3*), and  $0.13 \pm 0.01\%$  (*cyp-37A1; mbo-6*), showing a pattern of change consistent with fusion capabilities, albeit with low significance. The two identified PE(20/18) subspecies combined also show a similar pattern of change (Fig. 4c, e). Each class of phospholipid may also be divided into subclasses. A subclass is defined and measured by the number of carbon atoms and the number of double bonds of two fatty acyl tails combined, without knowing the identity of individual fatty acid. A subclass of phospholipid with carbon number  $\geq 38$  most likely contains at least one C20 PUFA. As shown by lipidomics, PC( $\geq 38$ ) decreases significantly in fusion-defective *cyp-37A1; fat-3* ( $8.96 \pm 0.29\%$  of total LD PC) and *cyp-37A1; mbo-6* ( $35.71 \pm 0.57\%$ ) compared to in *cyp-37A1* ( $55.91 \pm 0.28\%$ ). PC( $\leq 37$ ) increases complementarily in fusion-defective *cyp-37A1; fat-3* and *cyp-37A1; mbo-6* ( $91.04 \pm 0.29\%$  and  $64.29 \pm 0.57\%$  compared to  $44.09 \pm 0.28\%$ ) (Fig. S5a). These results are consistent with a positive role of FAT-3 and MBOA-6 in remodeling LD PC with C20 PUFAs.

PC( $\geq 38$ ) increases but little in fusion-competent *cyp-37A1* ( $55.91 \pm 0.28\%$  vs.  $54.76 \pm 0.89\%$  in WT) and decrease little in fusion-defective *cyp-37A1; daf-12* ( $53.51 \pm 0.84\%$  vs.  $55.91 \pm 0.28\%$  in *cyp-37A1*) (Fig. S5a). PE ( $\geq 38$ ) subclass shows no such a pattern (Fig. S5b). No subspecies or subclass of PI, PS, PA, PG, LPC, CL, LPE, and LPI shows a pattern closely correlated with fusion capabilities (Fig. S5c-j). We also conducted lipidomics to profile LD PC and PE subspecies of WT and *daf-12; fat-3*, and *mbo-6* single mutants. These single mutants do not show the same pattern of change as in *cyp-37A1* background. For example, molar percentages of PC(20/20) subspecies combined are  $1.97 \pm 0.05\%$  (WT),  $1.92 \pm 0.21\%$  (*daf-12*),  $0.10 \pm 0.01\%$  (*fat-3*),  $1.84 \pm 0.08\%$  (*mbo-6*). Except *fat-3*, *daf-12* and *mbo-6* are not significantly decreased in PC(20/20), PC(20/15+17), PC(20/18+19), or C20-PE subspecies (Fig. S6a-d). Taken together, these data imply that CYP-37A1 and DAF-12 oppositely regulate the LD targeting of FAT desaturases and MBOA-6 to effect on the synthesis of C20 PUFAs, particularly  $\omega$ -3 C20:4n3 and C20:5n3, and on the remodeling of mainly PC subspecies.

C20 PUFA-phospholipids increase the whole cell membrane fluidity in mammalian cells<sup>17,18</sup>. The increase and decrease of C20 PUFA-PC in LD membrane may also affect fluidity. We purified GFP::DGAT-2-labeled LDs from WT and fusion mutants and conducted fluorescence recovery after photobleaching (FRAP) experiments at  $-22\text{ }^{\circ}\text{C}$  in vitro to measure LD membrane fluidity (Fig. 4f). Fluorescence in the bleached LD membrane region recovers with different rates in WT and fusion mutants (Fig. 4g, h). The rate is expressed as t-half, time taken for recovering to half of the maximum. The t-half of fusion-competent *cyp-37A1* is  $1.70 \pm 0.43\text{ s}$ , significantly shorter than  $8.74 \pm 0.86\text{ s}$  of WT. The t-halves of fusion-defective *cyp-37A1; daf-12*, *cyp-37A1; fat-3*, and *cyp-37A1; mbo-6* are  $7.71 \pm 0.65\text{ s}$ ,  $5.91 \pm 0.85\text{ s}$ , and  $8.86 \pm 0.83\text{ s}$ , respectively, significantly longer than *cyp-37A1* (Fig. 4i). FRAP with LDs labeled by another LD marker DHS-3::GFP (*ssdSi7*) gave similar results (Fig. S7a-c). The t-half of fusion-enhanced *cyp-37A1; fat-4* ranges from 0.74 to 1.58 s (Fig. 4i; Fig. S7c), slightly shorter than that of *cyp-37A1* with no significance; the insignificance is likely due to the precision limit of FRAP experiment. These results show that C20 PUFA-PC increases LD membrane fluidity already at  $20\text{ }^{\circ}\text{C}$  in preparation for fusion at  $30\text{ }^{\circ}\text{C}$ . We note that the mobile fractions (recovery ratios) of fusion mutants range from 29% to 67% and do not necessarily correlate with t-halves or fusion capabilities (Fig. S7d, e). These mutants may also affect other physicochemical properties of LD phospholipids and the recovery ratios of the marker proteins.

### Decreasing LD membrane fluidity attenuates thermosensitive fusion

Dimethyl sulfoxide (DMSO) is a reagent that can reduce the fluidity of phospholipid bilayer membranes<sup>34-36</sup>. We grew WT and fusion mutants on NGM/OP50 media supplemented with 280 mM DMSO. GFP::DGAT-2-labeled LDs were purified and subjected to FRAP at  $22\text{ }^{\circ}\text{C}$ . The t-half values show that DMSO only slightly decreases LD membrane fluidity of WT ( $8.04 \pm 0.71$  vs.  $7.29 \pm 0.90\text{ s}$ ), but significantly decreases fluidity of *cyp-37A1* ( $4.08 \pm 0.48$  vs.  $2.00 \pm 0.40\text{ s}$ ) and *cyp-37A1; fat-4* ( $6.42 \pm 0.91$  vs.  $1.58 \pm 0.37\text{ s}$ ) (Fig. 5a-c). As shown by Oil Red O staining, 280 mM DMSO completely suppresses the thermosensitive fusion phenotype of *cyp-37A1*, specifically reducing LD size at  $30\text{ }^{\circ}\text{C}$  but not the regular small LD size at  $20\text{ }^{\circ}\text{C}$  (Fig. 5d, e). Moreover, 280 mM DMSO completely suppresses the enhanced thermosensitive fusion phenotype of *cyp-37A1; fat-4* at both  $20\text{ }^{\circ}\text{C}$  and  $30\text{ }^{\circ}\text{C}$  (Fig. 5f, g). The suppression effect of DMSO is dose dependent. The DMSO concentration at which 50% of the animals are not fusion positive,  $[\text{DMSO}]_{1/2}$ , is 105.63 mM for *cyp-37A1* and 129.21 mM for *cyp-37A1; fat-4* at  $30\text{ }^{\circ}\text{C}$  (Fig. 5h). The higher  $[\text{DMSO}]_{1/2}$  for *cyp-37A1; fat-4* than for *cyp-37A1* at  $30\text{ }^{\circ}\text{C}$  and the dose-dependent suppression of *cyp-37A1; fat-4* at  $20\text{ }^{\circ}\text{C}$  confirm that *cyp-37A1* and *fat-4* mutations potentiate fusion through the same DMSO-suppressible LD membrane fluidity mechanism.

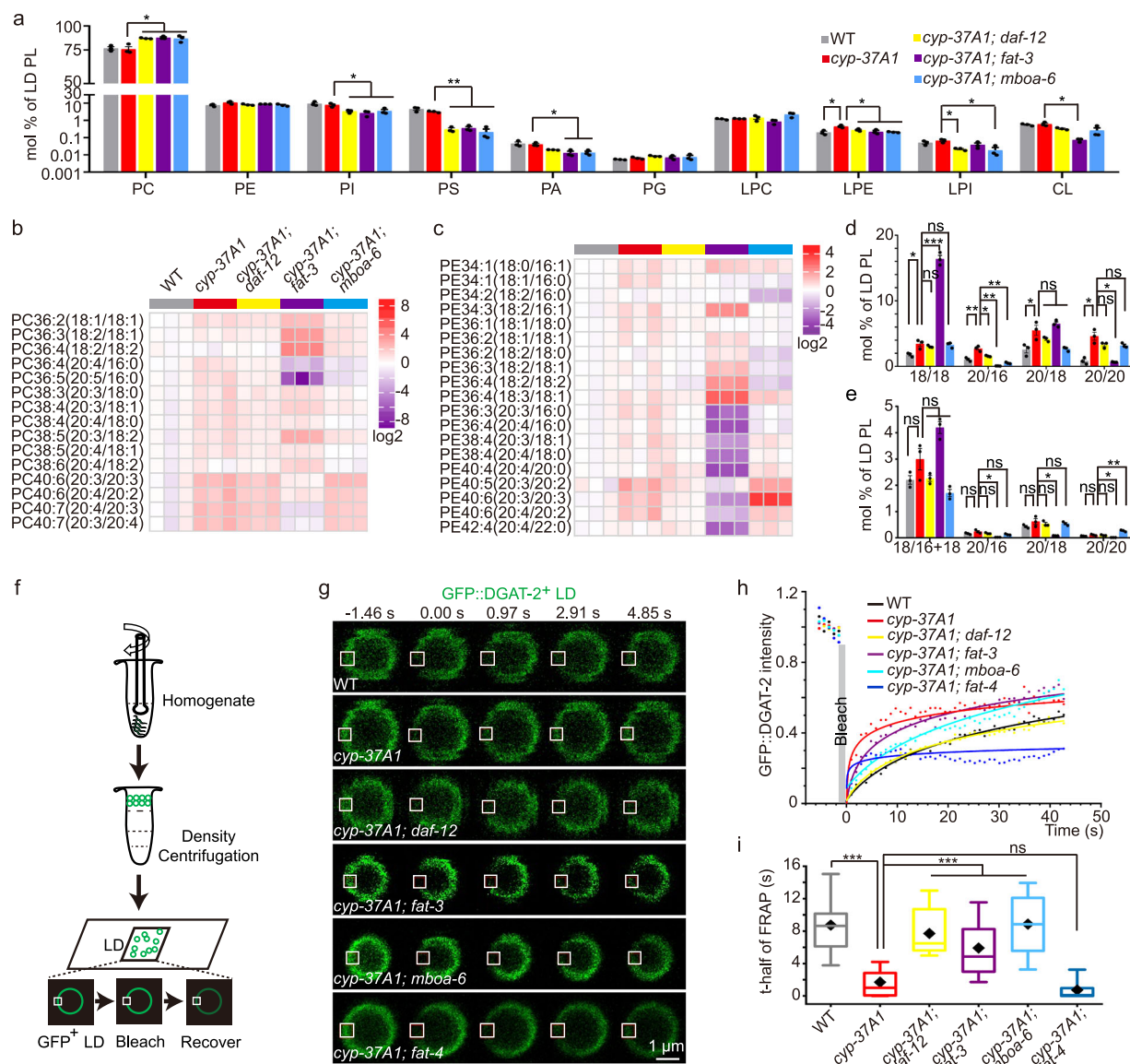


**Fig. 4 | Phospholipid compositions and membrane fluidity of LDs purified from thermosensitive fusion mutants.** **a** Molar percentages of major classes of glycerol phospholipids of LDs purified from WT and thermosensitive fusion mutants. Y axis is on the log10 scale. **b, c** Relative levels of PC and PE subspecies of purified LDs. PC36:2(18:1/18:1) refers to a PC subspecies with two C18:1 fatty acyl chains, etc. The molar percentages of triplicate LD samples of each mutant were normalized against the mean molar percentage of WT LDs, which was arbitrarily valued as 1. Data were exported as heat maps. **d, e** Molar percentages of PC and PE subspecies grouped according to chain lengths. The coloring scheme in (c–e) is the same as that in (a, b). In (a, d, e), each data column is mean  $\pm$  SEM.  $N = 3$  biological replicates. ns,  $P \geq 0.05$ . \*,  $P < 0.05$ . \*\*,  $P < 0.01$ . \*\*\*,  $P < 0.001$ . Unpaired two-sample two-tailed  $t$ -test. In (a),

differences uncorrelated with fusion capabilities or without significance are not labeled. **f** Flowchart of FRAP on purified GFP::DGAT-2-labeled LDs. **g** Representative FRAP images of LDs of WT and fusion mutants. White box, FRAP area. **h** Time course of FRAP of GFP::DGAT-2 fluorescence. Each line is the average of at least 20 individual FRAP data lines. **i**  $t$ -half values of FRAP.  $N = 20, 22, 23, 22, 25$ , and 20 LDs, respectively. Data are presented as box-whisker plot, which shows the lower extreme (10%), lower quartile, median, upper quartile, upper extreme (90%), and mean (diamond) values. For statistical tests, ns,  $P \geq 0.05$ . \*\*\*,  $P < 0.001$ . Unpaired two-sample two-tailed  $t$ -test. All exact  $P$ -values and source data of (a–e, h, i) are provided as Source Data file.

Moreover, the membrane fluidity of *cyp-37A1* LDs significantly increases with temperature, while that of WT LDs increases little (Fig. 5i).

As a negative control, LD size of WT is not significantly affected by DMSO at either 20 °C or 30 °C (Fig. S8a, c, e). Another negative control is the *daf-22* mutant, which is defective in peroxisomal fatty acid  $\beta$ -oxidation and results in supersized LD formation through the up-regulation of LD growth mediated by the TAG synthesis enzyme complex ACS-22-DGAT-2<sup>21,22,37</sup>. DMSO has no effect on the supersized LD phenotype of *daf-22* either (Fig. S8b, d, e). Moreover, *fat-3*, *mbo-6*, and *daf-12*, the three suppressor mutants of *cyp-37A1*, have little effect

on the LD growth phenotype of *daf-22* (Fig. S8f–j). Thus, the effect of DMSO and LD membrane fluidity on thermosensitive fusion is specific.

#### Dragging $\omega$ 3 desaturase FAT-1 or MBOA-6 to LDs enhances thermosensitive fusion

The LD targeting of FAT desaturases and MBOA-6 appears pivotal to remodeling LD membrane phospholipids for fusion. We found that lowering LD membrane fluidity by *fat-3* mutation or by dietary supplementation of 280 mM DMSO reduces LD targeting of transgenic MBOA-6::GFP protein (*ssdS26*) in *cyp-37A1* mutants (Fig. S9a, b, d). The reduction of LD targeting is not due to a reduction of expression,

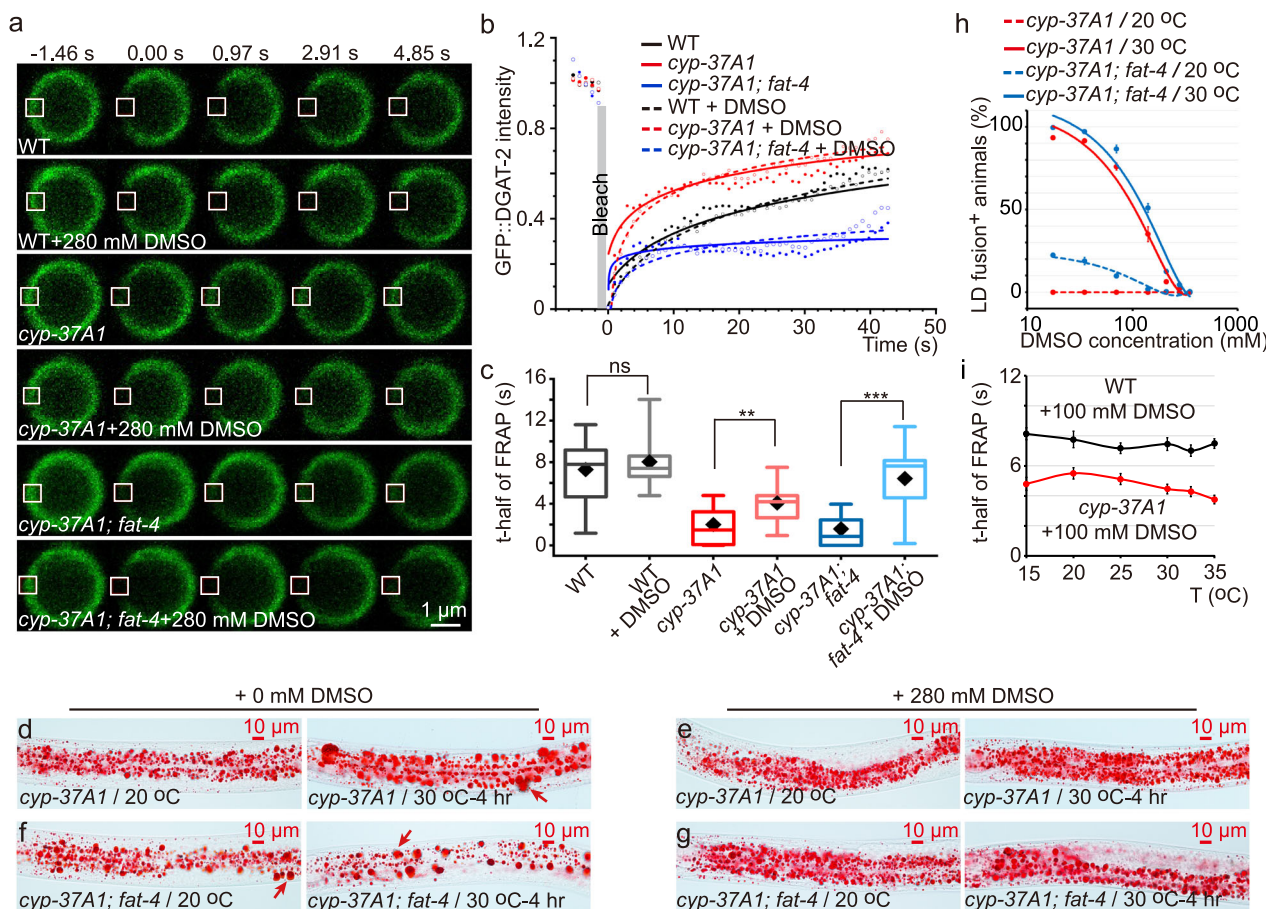


**Fig. 5 | Effect of LD membrane fluidity on thermosensitive fusion.** **a–c** Effect of DMSO supplementation on LD membrane fluidity. FRAP experiments with GFP:DGAT-2-labeled LDs purified from WT, *cyp-37A1*, and *cyp-37A1; fat-4*. White box, FRAP area. DMSO concentration was 280 mM in the NGM medium.  $N = 22, 25, 22, 25, 20$ , and  $17$  LDs, respectively. T-half values are presented as box-whisker plot, which shows the lower extreme (10%), lower quartile, median, upper quartile, upper extreme (90%), and mean (diamond) values (**c**). ns,  $P \geq 0.05$ . \*\*,  $P < 0.01$ . \*\*\*,  $P < 0.001$ . Unpaired two-sample two-tailed  $t$ -test. **d–g** Thermosensitive LD fusion phenotypes of *cyp-37A1* and *cyp-37A1; fat-4* without or with 280 mM DMSO supplementation. Oil Red O staining. Arrows point to supersized LDs resulted from

fusion. **h** Effects of graded concentrations of DMSO on thermosensitive LD fusion phenotypes of *cyp-37A1* and *cyp-37A1; fat-4*. DMSO concentrations were 17.5, 35, 70, 140, 210, 280, and 350 mM (X-axis, log10 scale). Each data point is the mean  $\pm$  SEM of three replicates, each of which consisted of more than 50 stage L4 animals.

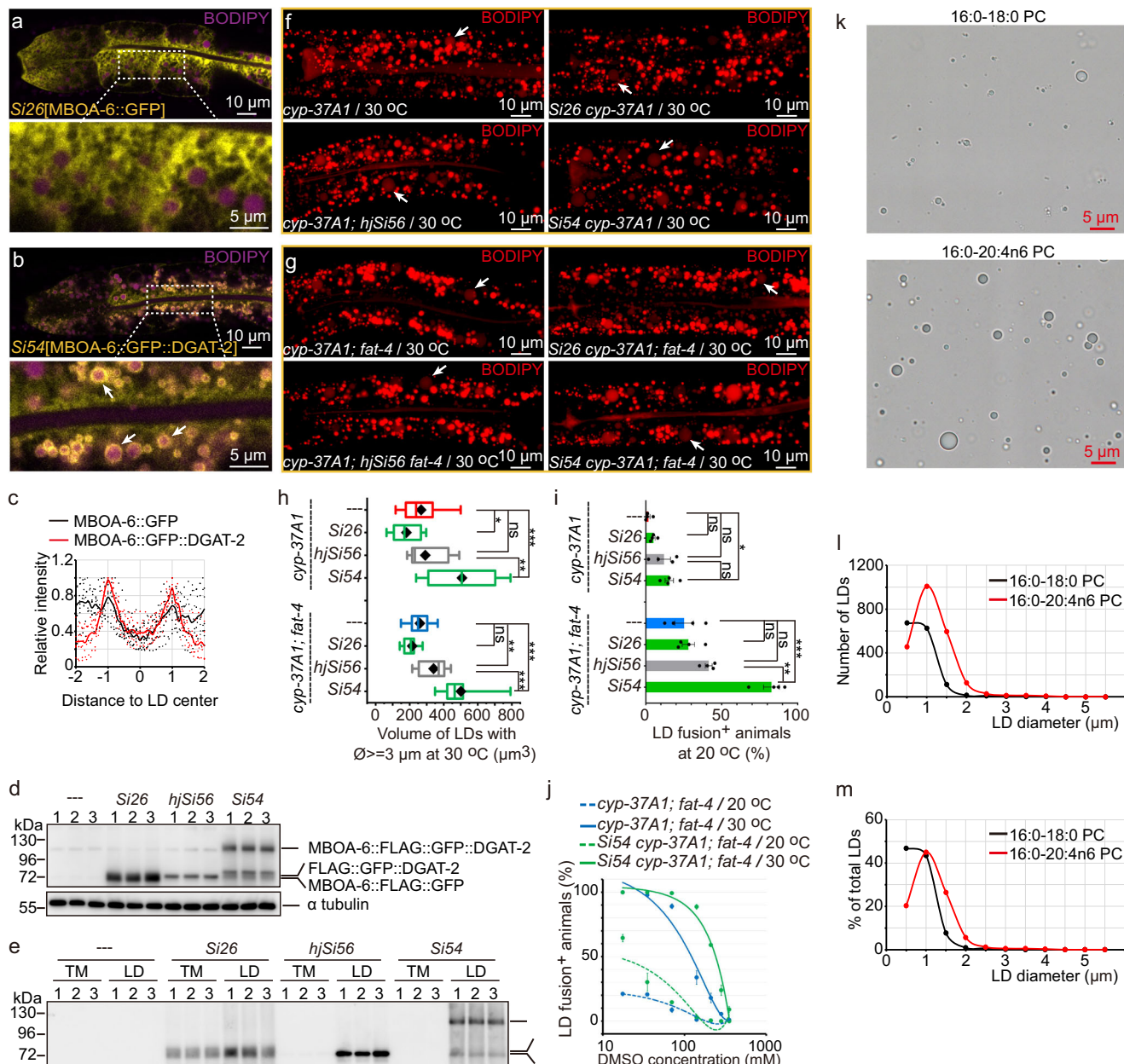
**i** Effect of temperature on membrane fluidity of LDs purified from WT and *cyp-37A1* animals supplemented with 100 mM DMSO. Data are mean  $\pm$  SEM. For WT,  $N = 56, 57, 57, 52, 55$ , and  $53$  LDs, respectively. For *cyp-37A1*,  $N = 57, 55, 55, 56, 54$ , and  $54$  LDs, respectively. All exact  $P$ -values and source data of (**b**, **c**, **h**, **i**) are provided as Source Data file.

which is not affected by *fat-3* mutation or DMSO (Fig. S9c). Similarly, the LD targeting of transgenic FAT-1::GFP (*ssdSi32*) and FAT-3::GFP (*ssdSi11*) in *cyp-37A1* is also reduced by *mbo-6* mutation and DMSO (Fig. S9e–h). It suggests that the high LD membrane fluidity resulted from these phospholipid desaturation enzymes in return increasing their targeting.

To directly test whether LD targeting plays an active role in fusion, we constructed a transgenic line (*ssdSi54*) expressing MBOA-6::FLAG::GFP fused with the LD marker protein DGAT-2. MBOA-6::GFP::DGAT-2 drastically localizes to LDs already in WT, while MBOA-6::GFP (*ssdSi26*) does not (Fig. 6a–c). *ssdSi26*, *ssdSi54*, and *hjSi56* (GFP::DGAT-2) were crossed into *cyp-37A1* and *cyp-37A1; fat-4*. As shown by western blot, although MBOA-6::GFP::DGAT-2 is expressed slightly less than MBOA-6::GFP (Fig. 6d), it localizes almost exclusively to LDs, the same as GFP::DGAT-2 and much better than MBOA-6::GFP (Fig. 6e). Consequently, MBOA-6::GFP::DGAT-2 renders the total volume of supersized LDs formed in *cyp-37A1* ( $507.26 \pm 50.56$  vs.  $267.00 \pm 31.96 \mu\text{m}^3$ ) and *cyp-37A1; fat-4* ( $500.94 \pm 37.65$  vs.  $259.85 \pm 19.97 \mu\text{m}^3$ ) at  $30^\circ\text{C}$  much larger; GFP::DGAT-2 and MBOA-6::GFP have little effect (Fig. 6f–h). Furthermore, at  $20^\circ\text{C}$ , MBOA-6::GFP::DGAT-2 enables *cyp-37A1* partly fusion positive ( $15.52 \pm 2.74\%$  vs.  $2.36 \pm 1.10\%$ ) and *cyp-37A1; fat-4* almost all fusion positive

( $82.73 \pm 5.20\%$  vs.  $25.29 \pm 6.12\%$ ), while GFP::DGAT-2 and MBOA-6::GFP have little effect (Fig. 6i). MBOA-6::GFP::DGAT-2 also increases  $[\text{DMSO}]_{1/2}$  for the half suppression of thermosensitive fusion of *cyp-37A1; fat-4* from  $121.3$  mM to  $236.44$  mM (Fig. 6j). Introducing MBOA-6::GFP::DGAT-2 into *cyp-37A1* increases the level of LD PC(20/20) subspecies ( $2.57 \pm 0.37\%$  vs.  $0.90 \pm 0.21\%$ ), PC(20/18 + 19) ( $3.66 \pm 0.51\%$  vs.  $2.58 \pm 0.47\%$ ), and PC(20/15 + 17) ( $1.22 \pm 0.15\%$  vs.  $0.73 \pm 0.13\%$ ). Introducing *fat-4* mutation also increases the level of LD PC(20/20) ( $4.54 \pm 0.45\%$ ), PC(20/18 + 19) ( $5.24 \pm 0.21\%$ ), and PC(20/15 + 17) ( $1.27 \pm 0.06\%$ ). However, introducing both MBOA-6::GFP::DGAT-2 and *fat-4* does not further increase C20 PUFA-PC (Fig. S10a, b). MBOA-6::GFP::DGAT-2 and *fat-4* have little effect on the level of LD C20 PUFA-PE (Fig. S10c, d). These results demonstrate that the LD-targeted MBOA-6 remodels PC with C20 PUFAs so as to promote fusion.

Even in WT background, MBOA-6::GFP::DGAT-2 induces thermosensitive fusion-LDs slightly larger than  $3 \mu\text{m}$  formed at  $30^\circ\text{C}$  ( $65.88 \pm 6.81$  vs.  $14.38 \pm 3.93 \mu\text{m}^3$ ). In *fat-4* mutant background, it induces thermosensitive fusion stronger ( $124.13 \pm 16.15$  vs.  $7.30 \pm 2.47 \mu\text{m}^3$ ) (Fig. S11a, b). When fused with DGAT-2, transgenic FAT-1 and FAT-3 also prominently localize to LDs already in WT (Fig. S11c–h). FAT-1::GFP::DGAT-2 (*ssdSi47*) also induces thermosensitive fusion in WT ( $30.09 \pm 5.48 \mu\text{m}^3$ ) and *fat-4* background



( $93.29 \pm 14.29 \mu\text{m}^3$ ) (Fig. S11a, b). FAT-1::GFP::DGAT-2 and FAT-3::GFP::DGAT-2 (*ssdSi45*) make *cyp-37A1* animals  $12.94 \pm 2.74\%$  and  $19.54 \pm 3.89\%$  fusion positive at 20 °C, while FAT-1::GFP and FAT-3::GFP do not. FAT-3::GFP::DGAT-2 does not increase the percentage of fusion positives of *cyp-37A1; fat-4* at 20 °C, while FAT-

1::GFP::DGAT-2 drastically increases it from  $27.20 \pm 1.53\%$  to  $54.72 \pm 12.39\%$  (Fig. S11i). These data show that targeting MBOA-6 or FAT-1 to LDs induces the fusion phenotype, and for a strong induction, a high temperature and sensitized genetic backgrounds of *cyp-37A1* and *fat-4* are required.

To further test the role of C20 PUFA-PC in LD fusion, we used a fusion assay of artificial LDs prepared *in vitro*<sup>12,14</sup>. The results showed that, compared to LDs prepared with PC(16:0/18:0), LDs prepared with PC(16:0/20:4n6) are more in number and much larger in size, presumably resulting from fusion (Fig. 6k–m).

### Human LPCAT3 localizes to LDs and positively regulates LD size and thermosensitive LD fusion

Mammals have  $\Delta 6$  desaturase FADS2 (homolog of FAT-3) and the PC-remodeling LPCAT3 (homolog of MBOA-6). Mammals do not have homologs of  $\omega 3$  desaturase. So for the synthesis of phospholipids containing C20 & C22  $\omega 3$  PUFAs, dietary C18:3n3 levels and FADS2 and LPCAT3 functions are critical<sup>38</sup>. However, the function of FADS2 and LPCAT3 in LD fusion has not been tested. We transiently expressed FADS2-GFP and LPCAT3-GFP fusion proteins in human HEK293T cell line. HEK293T cells were cultured in 10% fetal bovine serum/DMEM medium added with or without 600  $\mu$ M C18:1n9 to induce lipogenesis and LD formation. The results showed that FADS2-GFP localizes to LDs only under the lipogenesis condition. In contrast, LPCAT3-GFP localizes to LDs under the non-lipogenesis condition and more so under the lipogenesis condition (Fig. 7a–c). Under the non-lipogenesis condition, FADS2-GFP and the GFP negative control have no obvious difference in LD size distribution or the total LD volume per cell ( $1.32 \pm 0.14$  vs.  $1.15 \pm 0.13 \mu\text{m}^3$ ). However, LPCAT3-GFP increases the total LD volume per cell ( $1.86 \pm 0.17 \mu\text{m}^3$ ) with significance and increases the percentage and volume of LDs with diameter longer than 1  $\mu\text{m}$  ( $0.51 \pm 0.13$  vs.  $0.17 \pm 0.08 \mu\text{m}^3$ ) (Fig. 7d, e). Under the lipogenesis condition, LDs become more abundant and larger. However, compared with GFP ( $9.88 \pm 1.14 \mu\text{m}^3$ ), FADS2-GFP ( $10.05 \pm 0.94 \mu\text{m}^3$ ) and LPCAT3-GFP ( $10.88 \pm 1.39 \mu\text{m}^3$ ) do not increase the total LD volume significantly. The two proteins increase the volume of LDs longer than 1.5  $\mu\text{m}$  but not always with significance (Fig. 7f, g). From these data, it is concluded that the lipogenesis condition induces the targeting of FADS2 and LPCAT3 to LDs, and LPCAT3 plays a more important role than FADS2 in regulating LD size. As discussed in the introduction, LD growth, typical LD fusion, and atypical LD fusion all take place in the same mammalian cell during lipogenesis. It is not feasible to interpret LD size expansion as indicating LPCAT3 having a specific role in LD fusion in HEK293T cells.

To directly test the role of LPCAT3 in expanding LD size, a transgenic *C. elegans* line expressing LPCAT3::GFP (*ssdSi78*) was created and introduced into *cyp-37A1*, the mutant model of thermosensitive LD fusion. Similar to MBOA-6::GFP, LPCAT3::GFP localizes to LDs in *cyp-37A1* but not in WT or the fusion-defective *cyp-37A1; daf-12* (Fig. 7h, i). In addition to *ssdSi78*, two high-copy transgenic lines expressing higher levels of LPCAT3::GFP (*ssdEx105/106*) were created (Fig. 7j, k). These three lines rescue *cyp-37A1; mbo-6* double mutant, restoring thermosensitive LD fusion. The restoration is incomplete and is positively correlated with LPCAT3::GFP levels. The posterior intestine cells are restored better, probably due to differential activity or sensitivity between posterior and anterior intestine cells and between LPCAT3 and MBOA-6 (Fig. 7l, m). Taken together, human LPCAT3 is functionally orthologous to MBOA-6 in the respect that LPCAT3 localizes to LDs and facilitates thermosensitive LD fusion at least in *C. elegans*.

### Discussion

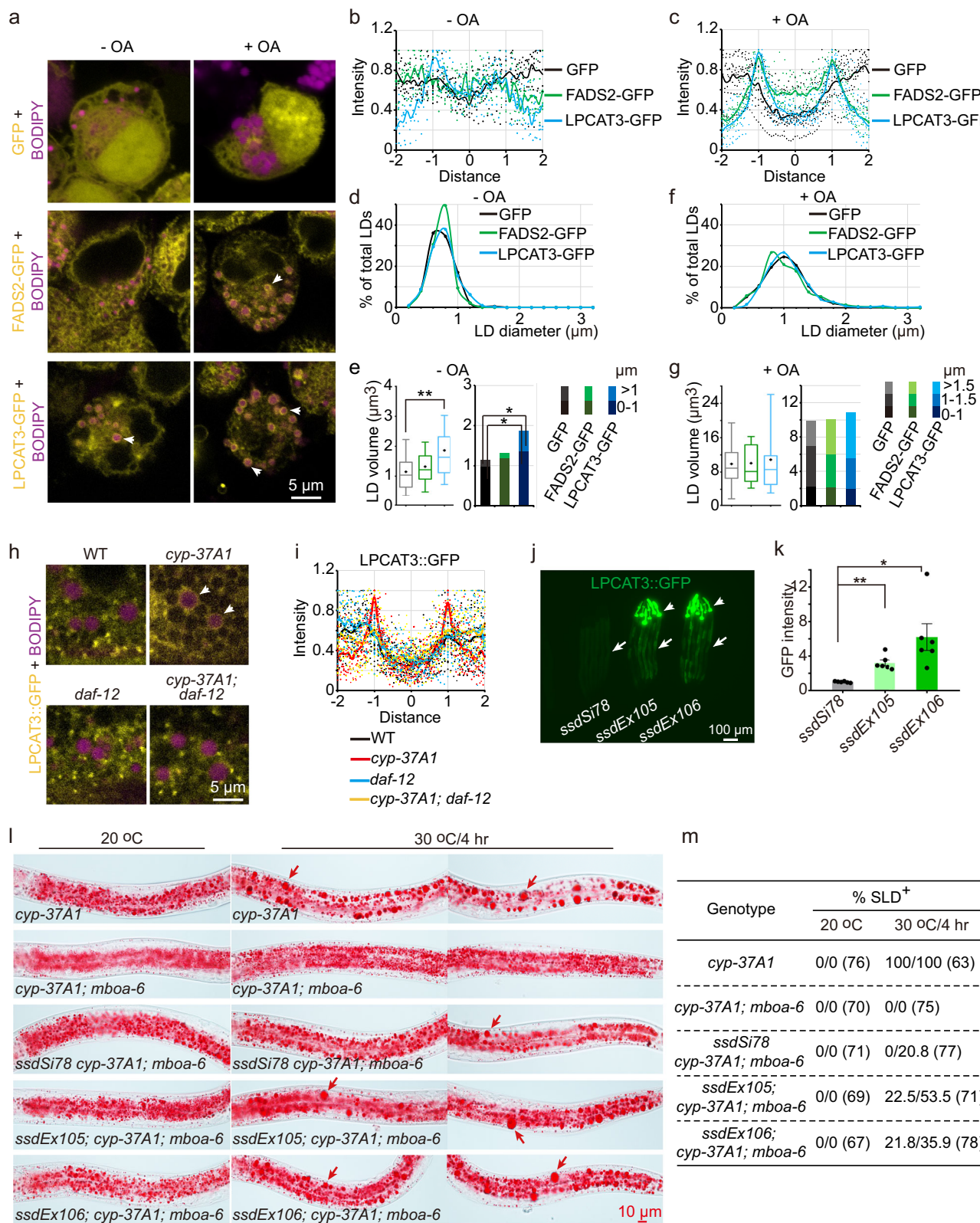
Although lipid droplet fusion has been studied for quite long, the role of LD membrane remains unclear. During atypical fusion in mammalian cells, how LD membranes are perforated by the Cide protein complex to permit TAG transfer is not understood<sup>7,9</sup>. In the yeast Seipin knockout model of typical fusion, the level of PA in LD phospholipids was not measured although the level of PA in total cellular phospholipids was found to increase by nearly two fold. A high molar percentage of 3–5% of PA in phospholipids of artificial LDs promotes

fusion *in vitro*<sup>14</sup>. In contrast, a low percentage of 0–10% of PC, as opposed to the normal level of 20%, promotes fusion of artificial LDs and of LDs in CCT1 knockdown *Drosophila* cells<sup>12</sup>. The unusually high PA and low PC levels in Seipin knockout and CCT1 knockdown cells and in artificial LDs are unlikely all the mechanisms underlying typical LD fusion. In mammalian LD phospholipids, the normal level of PA is estimated to be <1%, and that of PC is >50%<sup>39–41</sup>. During lipogenesis of cultured 3T3-L1 adipocytes, typical fusion and atypical fusion both occur<sup>3,4,13</sup>. However, PC and PE in LD phospholipids do not change; instead, C16 and C18 SFAs in PC/PE decrease while C18 MUFA in PC/PE and C20 PUFAs in PE significantly increase<sup>41</sup>. Intriguingly, in the Cide-overexpressing atypical fusion-active 3T3-L1 adipocytes, C18 SFA in LD PC increases<sup>42</sup>. In the Seipin knockout typical fusion-active yeast, C12, C14, and C16 SFAs in all major cellular phospholipids increase<sup>10</sup>. These inconsistent changes are difficult to reconcile with a role of unsaturated phospholipids in LD fusion but they do allude to such a possibility.

As mentioned previously, the Cide-overexpressing and CCT1 and Seipin knockdown/knockout cell models were investigated under lipogenesis conditions. As such, typical fusion, atypical fusion, LD growth, and LD de novo formation, and hence TAG levels, are inevitably up-regulated, and LD hydrolysis is down-regulated under these conditions<sup>3,43</sup>. These processes all affect the LD size phenotype, and it complicates the attribution of the phenotype to just one process. Another challenge in studying fusion processes is to specifically manipulate phospholipids and properties of LD membrane without perturbing other membrane systems. Many proteins and enzymes of lipid and LD metabolism are pleiotropic in cellular function, affecting other membrane organelles in addition to LDs. For example, CCT1 was found to localize to LDs growing without fusion and to ER<sup>20</sup>, suggesting additional roles in LD growth and in the proper function of ER. The typical fusion-implicated Seipin was shown to function in LD de novo formation and in other processes as well<sup>44–47</sup>.

The *C. elegans* mutants used in this study are a clean model of LD size alteration by thermosensitive fusion, with little changes in lipogenesis or TAG levels and no contribution from LD growth. Here, using precision lipidomics on purified LD samples, we show that in both WT and fusion mutants, PC is by far the most abundant LD membrane phospholipid, being about 75%, and PA is less than 0.1%. These levels are comparable with those in mammalian LDs. In the fusion-competent *cyp-37A1* mutant and the fusion-defective *daf-12*, *fat-3*, and *mbo-6* mutants, the levels of PC, PE, and PA change little or the changes do not correlate with fusion capabilities. What change significantly and correlate functionally with fusion capabilities are the levels of PC and PE containing C20 PUFAs, especially  $\omega 3$  C20 PUFAs. Furthermore, mutations of key enzymes for de novo PC synthesis have no major effect on thermosensitive fusion. Phospholipids remodeled with C20 PUFAs are known to increase the fluidity of bilayer membrane<sup>38</sup>. Our FRAP experiments on purified LDs showed that these remodeled phospholipids also increase the fluidity LD monolayer membrane. Interestingly, LD membrane fluidity of *cyp-37A1* mutants increases with temperature. The increased fluidity probably promotes phospholipid mixing of two opposing LD membranes at the high temperature for fusion. C20 PUFAs also enable bilayer membranes to adapt to deformation and curvature<sup>38</sup>. C20 PUFAs may enable such an adaptability of LD membrane and thus facilitate the formation of a negatively curved connecting membrane between two colliding LDs for thermosensitive fusion, the same as that proposed for typical fusion<sup>12,14,49</sup>. In either scenario, our results demonstrate a pivotal role of the desaturation of LD PC/PE in regulating thermosensitive fusion (Fig. 8).

Perhaps what is more interesting is that cytochrome P450 protein CYP-37A1 and nuclear receptor DAF-12 oppositely regulate the transcription and LD targeting of the majority of FAT desaturases and MBOA-6. TEM results showed that these enzymes can directly localize



to LD monolayer membrane. By genetically targeting FAT-1 and MBOA-6 to LDs, we were able to specifically manipulate LD phospholipid desaturation and membrane fluidity and reveal its role in thermosensitive fusion. This line of findings establishes a paradigm of how processes of fatty acid desaturation and phospholipid remodeling generally required for most membrane systems are regulated by nuclear receptor signaling to be co-compartmentalized onto a specific

type of organelles, the LDs (Fig. 8). In a second line of investigation, we showed that human FADS2 and LPCAT3 localize to LDs in HEK293T cells under lipogenesis condition, and, overexpressing LPCAT3 increases LD size. It is unclear whether LPCAT3 regulates LD size through fusion or remodels LD membrane PC and PE in HEK293T. Nevertheless, taking advantage of the *C. elegans* fusion model, we showed that LPCAT3 can specifically support thermosensitive LD

**Fig. 7 | Subcellular localization of human LPCAT3 and its effect on LD size in human cells and on thermosensitive LD fusion in *C. elegans*.** **a–c** Distribution of transiently expressed GFP, FADS2-GFP, and LPCAT3-GFP relative to LDs in HEK293T cells. +/- OA, oleic acid supplemented or not. LDs were labeled with red BODIPY. Arrowheads point to LDs encircled by fluorescent proteins.  $N=10$  LDs for each data line (**b, c**). **d–g** LD size distribution in HEK293T cells overexpressing the three proteins under “–OA” or “+OA” condition. The percentages of LDs with different diameters are plotted in (**d, f**). LD volume per cell (left) and LD volume of each diameter sector per cell (right) are plotted in (**e, g**). For “–OA” condition,  $N=30, 33$ , and  $33$  cells, respectively. For “+OA”,  $N=27, 36$ , and  $38$  cells, respectively. The LD volume per cell data are presented as box-whisker plots, which show the lower extreme (10%), lower quartile, median, upper quartile, upper extreme (90%), and mean (diamond) values. **h, i** Distribution of LPCAT3::GFP (*ssdSi78*) relative to LDs in WT *C. elegans* and LD fusion mutants. *glo-4* mutation was also

introduced. Arrowheads point to examples of LD localization (**h**).  $N=20$  LDs for each data line (**i**). **j, k** Expression levels of LPCAT3::GFP in *ssdSi78* and high-copy transgenic lines *ssdEx105/106* in *cyp-37A1; mbo-6* background. Measurements are fluorescence intensities of LPCAT3::GFP in intestine (arrows), which is distinct from GFP expressed by a transgenic co-marker (arrowheads). Data are mean  $\pm$  SEM.  $N=6$  animals. In (**j, k**),  $^*, P < 0.05$ .  $^{**}, P < 0.01$ . Unpaired two-sample two-tailed *t*-test. **l** LD fusion phenotypes of *cyp-37A1; mbo-6* and *cyp-37A1; mbo-6* rescued by *ssdSi78/ ssdEx105/ ssdEx106*. Oil Red O staining. For the  $30^{\circ}\text{C}$  condition, anterior and posterior halves of the same animal are shown. Arrows point to supersized LDs. **m** Quantification of the LD fusion phenotype. % SLD $^{+}$ , percentage of fusion-positive animals. Percentage values before and after slash are of anterior and posterior intestines, respectively. Values in parentheses are numbers of animals counted. All exact *P*-values and source data of (**b–g, i, k**) are provided as Source Data file.

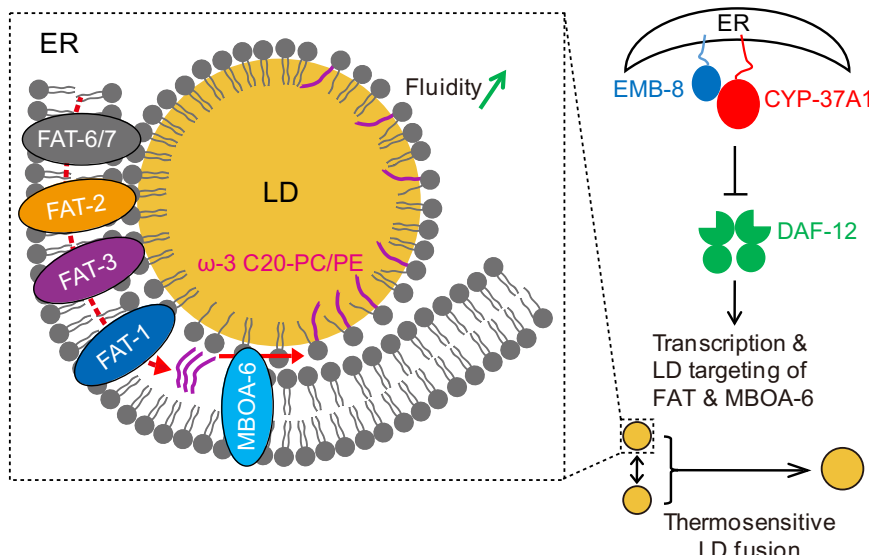


**Fig. 8 | Model of the regulation of thermosensitive LD fusion.** CYP-37A1 together with EMB-8 represses the function of DAF-12. When *cyp-37A1* is mutated, DAF-12 is relieved to up-regulate the transcription and LD targeting of most of the FAT

desaturases and MBOA-6. It leads to an increase of  $\omega$ -3 C20 PUFA-containing PC and PE and an increase of LD membrane fluidity, which is pivotal to thermosensitive fusion.

fusion in a dosage-dependent manner. These two lines of findings have implications for understanding mammalian LDs. LXR, the mammalian homolog of DAF-12, is activated under lipogenesis condition to up-regulate the transcription of LPCAT3<sup>50</sup>. LPCAT3 remodels cellular PC and PE with C20:4n6 to increase the overall cellular membrane fluidity, which functionally correlates with the secretion of lipoproteins out of enterocytes and hepatocytes; deleting LPCAT3 leads to excessive TAG accumulation and LD enlargement in mice<sup>17,18</sup>. Although the AGPAT family LPCAT1 and LPCAT2 are not the major enzymes for remodeling PLs with PUFAs<sup>19</sup>, the two enzymes can also localize to LDs and regulate LD size in cultured human cells by an unknown mechanism<sup>51</sup>. These results and ours suggest that compartmentalized phospholipid remodeling regulated by physiological nuclear receptor signaling may be a conserved mechanism underlying LD fusion. This mechanism echoes the compartmentalization of de novo PC synthesis and TAG synthesis for LD growth<sup>12,20,21</sup>, which is not known to be regulated by nuclear receptors though.

One limitation of this study is that it does not explain why  $\omega$ -3 C20-PC/PE are more conducive to fusion than  $\omega$ -6 C20-PC/PE, and why C20:4n3-PC/PE are more than C20:5n3-PC/PE. The double bond at  $\omega$ -3 position perhaps results in a more curved structure for the fatty acyl tails. This structure may disrupt the packing and increase the mobility of phospholipid molecules in LD membrane. Another limitation is that the exact mechanism by which MBOA-6/LPCAT3 and FAT

desaturases translocate from ER to LD is not revealed. Vertebrate LPCAT3 has two hairpins of  $\alpha$ -helices that traverse one leaflet of ER membrane<sup>52</sup>. Steroyl-CoA desaturase 1 (SCD1), the vertebrate ortholog of FAT-5/6/7, has three amphipathic  $\alpha$ -helices that anchor to the phospholipid heads of ER membrane<sup>53</sup>. The amino acid sequences of these hairpins and amphipathic  $\alpha$ -helices are highly conserved in MBOA-6 and FAT-5/6/7. These structures may mediate the translocation to LD membrane like the hairpins and amphipathic  $\alpha$ -helices in GPAT4 and CCT $\alpha$  do<sup>54</sup>.

Genetic experiments predict that CYP-37A1 synthesizes a lipophilic agent not identical to dafachronic acids to suppress DAF-12<sup>25,55</sup>. This prediction remains unproven and awaits biochemical identification of the CYP-37A1 product. CYP4V2, the human ortholog of CYP-37A1, was thought to  $\omega$ -hydroxylate and degrade C20 and C22 PUFAs<sup>56</sup>. How CYP4V2 mutation leads to the formation of lipid inclusions in RPEs is still unknown. A report suggested that lipid inclusions in human CYP4V2 mutant RPEs are autophagosomes<sup>57</sup>. However, several other reports showed that human, mouse, and zebrafish BCD mutant RPEs accumulate Oil Red O/Nile Red/BODIPY-positive globular structures, presumably LDs<sup>58–60</sup>. We previously showed that CYP4V2 represses thermosensitive LD fusion in *C. elegans* and we hypothesized that CYP4V2 does so in humans<sup>25</sup>. The current finding on LD membrane remodeling reinforces this notion and implies a role of LD fusion in the etiology of lipid inclusions in RPEs of human BCD patients.

## Methods

### *Caenorhabditis elegans* strains and growth condition

The wild-type strain was N2 Bristol. All strains were raised on standard 6 cm nematode growth medium (NGM) plates seeded with 200  $\mu$ L stationary phase liquid cultures of OP50 *Escherichia coli*. OP50 *E. coli* on the plates was allowed to grow at room temperature for 2–3 days before inoculating *C. elegans* strains. Animals were allowed to grow and proliferate on the plates at 20 °C. To induce thermosensitive LD fusion, plates were shifted to 30 °C and were incubated at 30 °C for 4 h. Mutants created or used in this study were: *cyp-37A1(ssd9)* II, *daf-12(m583)* X, *fat-3(ok1126)*, *ssd105*, *ssd127*, *ssd128*, *ssd146*, *ssd156*, *ssd252* IV, *fat-1(ok2323)* IV, *fat-2(wa17)* IV, *fat-4(ok958)*, *ssd338* IV, *fat-5(tm420)* V, *fat-6(tm331)* IV, *fat-7(wa36)* V, *mbo-6(ssd149)*, *ssd238*, *gk1217* III, *mbo-1(tm2464)* X, *mbo-2(ssd455)*, *ssd456* V, *mbo-3(tm1655)* X, *mbo-4(tm2967)* IV, *mbo-7(gk399)* X, *pcyt-1(et9)* X, *cept-1(et10)* X, *daf-22(ok693)* II, *glo-4(ok623)* V. Transgenic lines were: *ssdSi7[vha-6p::dhs-3::3xflag::tev::gfp]* II, *ssdSi11[vha-6p::fat-3::3xflag::tev::gfp]* II, *ssdSi24[vha-6p::fat-6::3xflag::tev::gfp]* II, *ssdSi25[vha-6p::fat-7::3xflag::tev::gfp]* II, *ssdSi26[vha-6p::mbo-6::3xflag::tev::gfp]* II, *ssdSi32[vha-6p::fat-1::3xflag::tev::gfp]* II, *ssdSi33[vha-6p::fat-2::3xflag::tev::gfp]* II, *ssdSi45[vha-6p::fat-3::3xflag::tev::gfp::dgat-2]* II, *ssdSi47[vha-6p::fat-1::3xflag::tev::gfp::dgat-2]* II, *ssdSi50[fat-5p::3xflag::tev::gfp]* II, *ssdSi52[fat-7p::3xflag::tev::gfp]* II, *ssdSi54[vha-6p::mbo-6::3xflag::tev::gfp::dgat-2]* II, *ssdSi78[vha-6p::LPCAT3::3xflag::tev::gfp]* II, *ssdEx105/106[vha-6p::LPCAT3::3xflag::tev::gfp]*, *hj156[vha-6p::3xflag::tev::gfp::dgat-2]* IV, *hj154[vha-6p::gfp::SP12]*, *hj153[vha-6p::gfp::daf-22]*. All strains with allele prefixes of *ssd* and *hj* were from our research group; others were obtained from the Caenorhabditis Genetics Center of USA and Mitani Lab through the National Bio-Resource Project of the MEXT of Japan. All mutant strains were backcrossed or outcrossed at least four times, and all transgenic *Si* and *Is* lines at least two times before phenotypic analysis. Double mutants and multiple mutants were constructed with standard genetic techniques.

### Molecular cloning of *drop-33* and *drop-35*

The *cyp-37A1(ssd9)*-Hawaiian strain was used to mate with *cyp-37A1(ssd9)* suppressor mutants to conduct single nucleotide polymorphism (SNP)-based three-point mapping<sup>25</sup>. Suppressor mutants *drop-35(ssd146)* and *drop-33(ssd149)* were mapped onto LG IV 4.93 to 6.44 map unit (physical location: 11,269,380–12,878,964) and LG III -16.11 to -15.3 map unit (physical location: 1,796,989 - 2,093,08), respectively. Genomic DNAs of the two strains were extracted and sent to Novogene (Beijing) for whole-genome re-sequencing and single-nucleotide variation and insertion-deletion analysis with reference to the WBcel215.69 release of *C. elegans* genome sequence and gene model annotation. In the mapped region of *drop-35(ssd146)*, a non-synonymous mutation of *fat-3* (c.CAG->TAG, p.Q174Amber) was found. The other five alleles were then Sanger sequenced, and all were found to harbor nonsynonymous mutations of *fat-3*. *drop-33(ssd149)* was found to harbor a nonsynonymous mutation of *mbo-6* (c.TGG->TAG, p.W443Amber). Another allele *drop-33(ssd238)* was Sanger sequenced and found to be mutated in the same site as *drop-33(ssd149)*.

### Creation of *fat-4* and *mbo-2* deletion alleles by CRISPR/Cas9

Single guide RNA (sgRNA) plasmid construction and CRISPR were conducted using standard procedures. Briefly, sgRNA sequences were designed using an online design tool (<http://crispr.mit.edu>), and higher-grade sequences were selected. For *fat-4*, two sgRNA sequences (GGGTTATGACTCTATTCAGATGG, GTCTCGCCAACAA-CATTTGTGG; PAM sequence is underlined) were designed against exon 4. For *mbo-2*, two sgRNA sequences (GCTCTCAAATTCATCT-CATATGG, GCATCATTGGACTGTAGATGTGG) were designed against exon 6. sgRNA sequences were cloned into a germline sgRNA expression vector pSOZ-105\_U6p:: sgRNA to obtain pSOZ-149 &

pSOZ-150\_U6p::fat-4 Exon 4 sgRNA and pSOZ-225 & pSOZ-226\_U6p::mbo-2 Exon 6 sgRNA. The two sgRNA constructs of each gene were injected together (each at a concentration of 50 ng/ $\mu$ L) with 50 ng/ $\mu$ L pSOZ-104\_eft-3p::cas9 and two other co-injection marker plasmids. pSOZ-149 and pSOZ-150 were injected into the gonad of *cyp-37A1(ssd9)*; *fat-3(ok1126)* young adult animals to obtain three *fat-4* mutants *ssd338*, *ssd339*, and *ssd340*, which are linked closely to *fat-3(ok1126)*. pSOZ-225 and pSOZ-226 were injected into *cyp-37A1(ssd9)* animals to obtain two *mbo-2* mutants *ssd455* and *ssd456*.

### Construction of *fat* gene promoter reporter lines

To examine promoter activities, *fat-5* and *fat-7* promoters (a 2000 bp sequence immediately upstream of the translation start codon) were PCR amplified from WT genomic DNA using primers SOZ-764F1/R1 and SOZ-766F1/R1, respectively. The PCR products were then cloned into a pCFJ151 vector containing the 3xflag::tev::gfp cassette using homologous recombination, to obtain pSOZ-311\_fat-5p::3xflag::tev::gfp and pSOZ-313\_fat-7p::3xflag::tev::gfp. The two constructs were injected at 50 ng/ $\mu$ L into EG6699 MosSCI targeting strain to obtain single-copy integrated lines: *ssdSi50* (pSOZ-311) and *ssdSi52* (pSOZ-313).

### Construction of transgenic lines expressing FAT, MBOA-6, and human LPCAT3 proteins

To characterize the subcellular localization pattern of FAT-3 protein, plasmid pSOZ-163\_vha-6p::fat-3::3xflag::tev::gfp was constructed. Briefly, *fat-3* cDNA (without stop codon) was PCR amplified with primers SOZ-444F2/R3 from 1st strand cDNA of WT. The PCR product was cloned into a pCFJ151 vector containing the vha-6p::3xflag::tev::gfp cassette using restriction sites SbfI and NotI to obtain pSOZ-163. Similarly, *fat-1*, *fat-2*, *fat-6*, *fat-7*, and *mbo-6* cDNA were PCR amplified with primers SOZ-671F1/565R1, SOZ-745F1/R1, SOZ-563F1/R1, SOZ-0718F1/R1 and SOZ-652F1/R1, respectively. PCR products were cloned into pSOZ-163 using the same restriction sites SbfI and NotI to obtain pSOZ-239\_vha-6p::fat-1::3xflag::tev::gfp, pSOZ-295\_vha-6p::fat-2::3xflag::tev::gfp, pSOZ-199\_vha-6p::fat-6::3xflag::tev::gfp, pSOZ-284\_vha-6p::fat-7::3xflag::tev::gfp, and pSOZ-227\_vha-6p::mbo-6::3xflag::tev::gfp. To make constructs expressing FAT-3 and FAT-1 proteins fused to DGAT-2, *dgat-2* cDNA was PCR amplified with primer SOZ-751F1/R1. Using homologous recombination, *dgat-2* cDNA was cloned into pSOZ-163 and pSOZ-239 to obtain pSOZ-298\_vha-6p::fat-3::3xflag::tev::gfp::dgat-2 and pSOZ-317\_vha-6p::fat-1::3xflag::tev::gfp::dgat-2. *mbo-6* cDNA was cut from pSOZ-227 and cloned into pSOZ-317 using restriction sites SbfI and NotI to obtain pSOZ-323\_vha-6p::mbo-6::3xflag::tev::gfp::dgat-2. To express human LPCAT3 in *C. elegans*, plasmid pSOZ-351\_vha-6p::LPCAT3::3xflag::tev::gfp was constructed. Briefly, LPCAT3 cDNA was PCR amplified with primer SOZ-818F1/R1, then cloned into pSOZ-163 using restriction sites SbfI and NotI to obtain pSOZ-351. The above constructs were injected at 50 ng/ $\mu$ L into EG6699 MosSCI targeting strain to obtain single-copy integrated lines: *ssdSi11* (pSOZ-163), *ssdSi24* (pSOZ-199), *ssdSi25* (pSOZ-284), *ssdSi26* (pSOZ-227), *ssdSi32* (pSOZ-239), *ssdSi33* (pSOZ-295), *ssdSi45* (pSOZ-298), *ssdSi47* (pSOZ-317), *ssdSi54* (pSOZ-323), and *ssdSi78* (pSOZ-351). Two Ex lines *ssdEx105/106* were obtained by injecting pSOZ-351 at 50 ng/ $\mu$ L into *cyp-37A1(ssd9)*; *mbo-6(ssd238)*.

### Primers for constructs

Primers are forward/reverse, 5'→3'. Sequences underlined are recognition sites of restriction enzymes in parentheses.

SOZ-444F2/R3:

GTCTCGCAGG(SbfI)ATGGTCGTCGACAAGAAT/ATGGCGGCCG  
(NotI)GGCAGCTTAGCTGAATGTGC

SOZ-671F1/565R1:

GTCTCGCAGG(SbfI)ATGGTCGTCATTCCTCAGAAGGGT/ATGGCGGCCG(NotI)CTTGGCCTTGCCCTCTCCT

SOZ-745F1/RI:  
GTCCTGCAGG(SbfI)ATGACAATCGCTACAAAAGT/  
ATGCGGCCGC(NotI)TTGAGCCTCTTAGCCTTG  
SOZ-563F1/RI:  
GTCCTGCAGG(SbfI)ATGACGGTAAAAACTCGT/ATGCGGCCGC  
(NotI)TCATGATTGATTTCTCGT  
SOZ-718F1/RI:  
GTCCTGCAGG(SbfI)ATGACGGTAAAAACTCGCGAGCA/  
ATGCGGCCGC(NotI)CATGATCGATTTCTTGATTCTCA  
SOZ-652F1/RI:  
ATCCTGCAGG(SbfI)ATGGCCGTAGTCGGAGCACT/  
ATGCGGCCGC(NotI)GAGCTCTTCTTGACTTCTT  
SOZ-764F1/RI:  
TTGCACTTATAATACGACTCACTAGTTAGCTCCAGGCCCTGG  
TAA/ TGTAGTCCATAGATCTGCCCCCTGCAGGTCTGGAAATTG  
AAGAATTTAGTTTC  
SOZ-766F1/RI: TTGCACTTATAATACGACTCACTAGTACACAGTT  
TACATGTAGTATT/TGTAGTCCATAGATCTGCCCCCTGCAGGT  
TACCGTTGTTCTGAAAG  
SOZ-751F1/RI:  
TTACACATGGCATGGATGAGCTAGCCCTAAACTACCAAATTCA  
CAAAAGCTACCGAC/TCCGGATTACTTGTATGCCCTGAAA  
AACGAGCCGAGTCCTG  
SOZ-818F1/RI:  
AACCTGAGG(SbfI)ATGGCGTCCTCAGCGGA/ATGCGGCCGC  
(NotI)TTCCATCTTCTTAACCTT

### Quantitative RT-PCR

Synchronized late L4 stage animals grown continuously at 20 °C on a standard 6 cm-NGM/OP50 plate were harvested as a biological replicate. Three replicates for each genotype. Total RNA was isolated using TRIzol (Invitrogen), and then reverse transcribed into 1st strand cDNA using ImProm-II RT kit (Promega). Quantitative real-time PCR was conducted using TB green (Takara) on a CXF96 Touch instrument (Bio-Rad). Relative mRNA levels were calculated using the  $\Delta\Delta Ct$  method, with *rpl-26* as an internal calibration control.

### qRT-PCR primers

Primers are forward/reverse, 5'→3'.

*rpl-26*: GCTATTCCAATCAGAACCGATGATG/CAGTGGATCCGTTA  
GCCTCT  
*tbb-2*: GAGGAGGAACCGATCTGAAT/GGCCTCGTTGCAATGC  
AGTAG  
*fat-1*: TGGACATATCGCTTCTCAC/TGGTGAAGCATGGTGAAG  
*fat-2*: GTCCTCTCGCACTATTCTGTC/GCTTCTGAGACCTCAATA  
TCC  
*fat-3*: CACTTCGGGTTGCTTATTTC/TTCGAGAATTGGCTGGATAC  
*fat-4*: ATGGATGCCACTACCGTATTC/GGGATCTCTGGTTCTGTC  
TAG  
*fat-5*: GGTGGACTATATCAGCTTG/CATGAGAGGGTGGCTTT  
GTAG  
*fat-6*: CATTCCGTTATTGCTTCACAC/GCTTCCATCCGAAATAGT  
GAG  
*fat-7*: TCCAGAGAAAGCACTATTCC/AGTGTGAAACAATAACGG  
AATG  
*daf-12*: TCCGTCAACGTGGATGATATG/GTCGAAGAAACCGAAGA  
ACTCTA  
*mbo-1*: ATGTGAAACGACGAGAATCGC/CGTTTTCAAGTCTCG  
GATAGC  
*mbo-2*: GGACGTACAGGAAACATCAT/TGAACTGCTGAAACACCA  
AAG  
*mbo-3*: CTGTTTGGAAAGGGCTATCAA/TCGAGAATAGCCCCATCG  
ATAG  
*mbo-4*: CGCCTGGACAATTCTGACTC/AGCCAGGCAACAGTCCA  
AATA

*mbo-6*: AGAGGGAAATGATAGATGGGA/TATTGTTAACCCACGG  
AGAC  
*mbo-7*: ATCACGAACCACTATTCCCA/GCAATTGCCAGGCAC  
GTAT  
*mom-1*: AGCACTCAAGCATTGTGTTG/CATGCAGTGAATTGA  
ACAAC  
*hhat-1*: GTACTCAAAGGTGGAGAG/CCTATCCAGACAATGTT  
TGA  
*hhat-2*: CGATGCGGAATGGCTTATT/GCATTGAAACTGCTCA  
TGT  
*elo-1*: GGAATTGTCGCATCCTACTG/CAGGGTAGATCATGTC  
GAG  
*elo-2*: TTGCCGTCCACACTGTTATG/CACATTCCAGCTAACAGCGC  
*elo-5*: GGATTTAGTCACACCTATTCCC/CGGTCAATGCCGTATGG  
TAC

### LD labeling, imaging, size measurement, and counting fusion-positive animals

Postfix Oil Red O staining, vital BODIPY staining, and optical imaging were essentially the same as previously described<sup>24,25</sup>. All samples were mid L4 stage hermaphrodites grown at 20 °C or shifted from 20 °C to 30 °C for 4 h if not otherwise indicated. For Oil Red O staining, 50 to 100 animals were fixed with paraformaldehyde and then stained with Oil Red O (Sigma, # O0625). More than 20 animals were imaged under a Nikon ECLIPSE Ni-E wide-field compound microscope. A typical image is presented, which shows the anterior half of the animal with head to the left. To measure the sizes of LDs vital labeled by green C1-BODIPY 500/510-C12 (Thermo Fisher, #D3823) or red BODIPY-558/568-C12 (Thermo Fisher, #D3835), channel mode fluorescence images of 10–20 animals were acquired using a Zeiss LSM780 inverted confocal microscope equipped with a Plan-Apochromat 63X/NA 1.40 Oil DIC M27 objective. A Z-stack image (9  $\mu$ m, slice interval 0.45  $\mu$ m) of the anterior half of each animal was acquired. A typical Z-stack image is presented as an extended focus view. To quantify the supersized LD/fusion phenotype, confocal images were rendered in 3D in the Zeiss Zen software. BODIPY-positive supersized LDs (with diameters of  $\geq 3$   $\mu$ m) in the two cells of the second intestine segment were labeled and measured. The volume of each supersized LD was calculated as  $\pi \times (\text{diameter}/2)^3 \times 4/3$ . The total volume of supersized LDs in the second intestine segment of each animal was summed. The mean volume of the 10–20 animals was calculated and plotted. To count the percentage of fusion-positive animals, 50–100 mid L4 stage animals were randomly picked from a fully grown 6 cm-NGM/OP50 plate of each desired mutant. The mid L4 stage animals were then inspected under a Nikon SMZ1500 stereo microscope. Supersized LDs were readily visualized as light-refracting globular structures greater than 4  $\mu$ m in diameter in the bright field at 180X magnification. An animal with at least two supersized LDs in the whole intestine was counted as supersized LD/fusion-positive. Genotypes for comparison were usually counted in parallel and in double-blind manner. Some of the counting results were verified by counting postfix Oil Red O stained animals under the Nikon ECLIPSE Ni-E compound microscope.

### TAG measurement and fatty acid profiling

For TAG measurement, 8000 synchronized freshly hatched L1 stage animals were seeded on a 10 cm NGM/OP50 plate. Animals were allowed to grow to late L4 stage and were collected as one replicate sample. One eighth of the sample was spared for protein extraction and measurement using BCA Protein Assay Kit (Pierce). The other seven eighths were homogenized, and 20  $\mu$ g tri-C17:0 TAG (Nu-Chek) was added as an internal calibration standard. Total lipids were extracted, and TAG was separated from other lipid species on a thin-layer chromatography plate. The TAG fraction was then transmethylated in 2 mL methanol with 50  $\mu$ L sulfuric acid. Fatty acid methyl esters (FAMEs) were extracted, re-dissolved in 2 mL pentane, and chromatographed using a GC-MS instrument (SHIMADZU,

QP2010 Ultra) or a GC-FID instrument (Agilent, HP7890A) with a DB-23 GC column (Agilent, 122-2332). FAME peaks were identified according to FAME standards. To calculate TAG mass, the areas of TAG FAME peaks were integrated and divided by the area of calibration standard C17:0 FAME. TAG mass was then divided by total protein mass to obtain the final normalized TAG level. For total fatty acid analysis, 4000 synchronized late L4 stage animals were collected as one replicate sample. Animals were homogenized and then directly transmethylated. FAMEs were extracted and subjected to GC/MS. The mass percentage of each fatty acid was calculated as peak area divided by the total peak area of all fatty acids.

### Fatty acid supplementation

Fatty acid supplementation experiments were conducted on 3.5 cm NGM/OP50 plates. Each 3.5 cm plate was poured with 3 mL NGM, seeded with 150  $\mu$ L OP50 *E. coli*, and grown at room temperature for 3 days. The four fatty acids used for supplementation were C20:3n6 (Nu-Check, #U-69A), C20:4n6 (Nu-Check, #U-71A), C20:4n3 (Cayman, #90011), and C20:5n3 (Nu-Check, #U-99A), all in the acid form. Each fatty acid stock was dissolved in pure ethanol, and before use, was diluted in 1X phosphate buffered saline to a volume of 60  $\mu$ L. The diluted stock was added uniformly onto the surface of the OP50 lawn. The final concentration of each fatty acid was 0.33 mM in the 3 mL NGM; the final concentration of carrier ethanol was 0.3% to 1.8% (V/V). As a negative control, ethanol was added to the plate at a final concentration of 1.8%. The plate was then dried immediately in a laminar flow hood. Fifteen synchronized stage L4 animals were inoculated onto the plate to develop and proliferate. Mid L4 stage progeny were picked out and subjected to staining and counting experiments.

### Measurement of GFP levels of *fat* gene promoter lines

To measure the expression levels of GFP reporter driven by the *fat* gene promoter in WT and thermosensitive fusion mutants, six L4 stage animals of each genotype were mounted on an agarose-padded slide. Two WT animals with no transgenes were mounted on the same slide. Animals were imaged with a Plan-Apo 10X/NA 0.45 air objective on the Nikon ECLIPSE Ni-E wide-field microscope. GFP fluorescence intensity in the intestine was measured using the NIS-Elements AR software. The mean background fluorescence of WT was subtracted from the fluorescence of each animal.

### Western blot of total proteins

For the Western blot of total proteins, 1000 late L4 stage animals were collected as one replicate. At least two replicates were collected. Total soluble proteins were extracted. An equal mass of each protein sample was loaded onto and separated by SDS-PAGE (polyacrylamide gel electrophoresis). Blotting, antibody incubation, and chemiluminescence assay were conducted according to standard procedures. Primary antibodies used were mouse anti-Flag monoclonal antibody (ABclonal, China, #AE005), mouse anti-GFP monoclonal antibody (TransGen, China, #HT801), and mouse anti- $\alpha$ -Tubulin monoclonal antibody (EASYBIO, China, #BE0031), all at 1/6667 dilutions. Primary antibody mouse anti-ATP5A (*C. elegans* ortholog ATP-1) (Abcam, UK, #ab14748) was at 1/5000 dilution. The secondary antibody was HRP-conjugated goat anti-mouse IgG antibody (EASYBIO, # BE0102) at 1/6667 dilution.

### Quantification of LD-localized GFP fusion proteins by in vivo imaging

The various transgenic lines expressing GFP and FAT/MBOA-6/LPCAT3 fusion proteins were crossed into thermosensitive fusion mutants. The *glo-4(ok263)* mutation was also brought into these mutants to eliminate LROs. Animals were vital stained by red BODIPY. More than 12 L4 stage animals were imaged under the Zeiss LSM780 inverted confocal microscope equipped with a Plan-Apochromat 63X/1.40 Oil DIC M27

objective. A Z-stack channel mode fluorescence image with 0.45  $\mu$ m intervals of each animal was taken. The distribution of GFP fusion proteins in relation to LDs was measured in the ImageJ software. A line segment was drawn across the center of a randomly picked red BODIPY-labeled LD. The LD center was defined as coordinate "0" and the circumference as "-1" and "+1" on the X-axis. GFP fluorescence intensity on the line segment was measured. The highest value on the line was taken as 1, and others were normalized against it.

### LD purification

LD samples were purified for the purposes of in vitro imaging and Western blot of LD-localized transgenic GFP fusion proteins, LD membrane phospholipid analysis, and LD membrane fluidity measurement. Briefly, freshly hatched L1 animals were grown to 1-day-adult stage on 15 cm-NGM/OP50 plates, 10,000 animals per plate. About 80,000 animals were harvested as one replicate sample. Each sample was washed three times with 1X PBS/0.001% Triton X-100 (PBST), one time with 1X PBS, and then with 4 mL buffer A [25 mM Tricine, pH 7.6, 250 mM sucrose, one protease inhibitor cComplete Tablet (#04693132001, Roche) per 50 mL volume]. The sample was resuspended in 4 mL buffer A and homogenized by 50 strokes in a Dounce homogenizer. Each homogenate was transferred into a 15 mL centrifuge tube and added with buffer A to 10 mL. The homogenate was centrifuged at 1000  $\times g$  for 10 min at 4 °C. A volume of 9 mL post-nuclear supernatant (PNS) was loaded into a 13 mL centrifuge tube. 3 mL buffer B (20 mM HEPES, pH 7.4, 100 mM KCl, and 2 mM MgCl<sub>2</sub>) was gently added on top of the 9 mL PNS. The sample was then centrifuged in a Beckman SW40 Ti rotor at 28,413 g for 1 h at 4 °C. The white top layer in the tube was carefully collected as the LD fraction; 2 mL transparent fraction in the lower layer was collected as the TM fraction. The LD fraction was washed three times with buffer B and centrifuged at 15,000  $\times g$  for 3 min at 4 °C. The TM fraction was centrifuged in a TLS-55 rotor at 100,000  $\times g$  for 1 h at 4 °C. The TM pellet was also washed three times with buffer B.

### Dot blot Coomassie staining

0.3  $\mu$ g of each LD and TM protein sample was dotted directly onto a methanol-activated PVDF membrane. Care was taken to ensure that the dotted membrane area for each sample was the same. The membrane was incubated at 37 °C for 30 min and then stained at room temperature with 0.1% Coomassie Brilliant Blue R-250 dye for 1 h on a horizontal shaker. The membrane was destained for 2 h, during which the destaining buffer was changed three times, and then photographed.

### Quantification of LD-localized GFP fusion proteins by in vitro imaging of purified LDs

From 1-day-adult stage animals of the various transgenic lines, LDs were purified as described above. The purified LD sample was immediately injected into the slit of a hemocytometer covered with a cover slip. The hemocytometer was mounted onto the Zeiss LSM780 confocal microscope and was imaged with a Plan-Apochromat 40X/0.95 air objective. About 10 random areas of the hemocytometer were sampled. For each area, a single-section channel mode confocal image was acquired. LD samples for direct comparison were imaged in the same setting. GFP fluorescence intensity of a given LD was measured in Image J software and was normalized by LD circumference. For each LD sample, more than 100 GFP-positive LDs were measured, and values were averaged.

### Quantification of LD-localized GFP fusion proteins by western blot of purified LD and TM proteins

LD and TM samples were purified from 1-day-adult stage animals of each transgenic line. To each LD or TM sample, 1 mL acetone was added. The sample was vortexed vigorously, chilled at -20 °C for 1 h,

then centrifuged at 15,000  $\times g$  for 10 min. Protein was spun down as a pellet. The protein pellet was air-dried and then dissolved in 30  $\mu$ L 2X SDS buffer. TM protein and LD protein were loaded at equal mass onto SDS-PAGE. Western blot procedures were described in the previous section.

### Phospholipid analysis

For phospholipid analysis, LDs from 100,000 1-day-adult stage animals were purified as one replicate sample. Three samples for each genotype. Each LD sample was added with 1 mL acetone, chilled at -20 °C for 1 h, and centrifuged at 15,000  $\times g$  for 10 min. The supernatant acetone fraction was collected as the LD total lipid sample. Lipidomics analyses were conducted at LipidALL Technologies (Changzhou, China) using an Exion-UPLC coupled with a 6500 PLUS QTRAP (Sciex). Briefly, lipids were re-extracted from the submitted sample using the improved Bligh/Dyer extraction method. Lipid samples were then remixed with isotope-labeled standards. Separation of individual lipid classes of polar lipids by normal phase (NP)-HPLC was carried out using a TUP-HB silica column (i.d. 150  $\times$  2.1 mm, 3  $\mu$ m) with the following conditions: mobile phase A (chloroform: methanol: ammonium hydroxide, 89.5:10:0.5) and mobile phase B (chloroform: methanol: ammonium hydroxide: water, 55:39:0.5:5.5). The mobile phase A gradient was started at 95% and maintained for 5 min, linearly decreased to 60% within 7 min and maintained for 4 min, and then further decreased to 30% and remained for 15 min. Finally, the initial gradient was held for 5 min. Multiple reaction monitoring (MRM) transitions were set up for comparative analysis of various polar lipids. Individual lipid species were quantified by referencing to spiked internal standards. Standards DMPC, DMPE, d31-PS(d31-16:0/18:1), C17-PA, DMPG, d1c8-PI, Cardiolipin MIX I (CL86:4; CL80:4; CL61:1; CL57:4), d7-LPC18:1, C17-LPE, C17-LPI were from Avanti Polar Lipids.

### Transmission electron microscopy of purified LDs

For TEM, LDs were purified using a simplified protocol. Briefly, 30,000 1-day-adult stage animals were collected in a 1.5 ml Eppendorf tube, washed, and homogenized in 1X PBS using an electric pellet pestle. After centrifugation at 15,000  $\times g$  for 3 min, LDs floated to the top layer/fraction. The lower layer and precipitate were carefully aspirated using a long pipette tip and were discarded. LD fraction was washed three times with 1X PBS and centrifuged at 15,000  $\times g$  for 3 min at 4 °C; the lower non-LD fraction was removed as much as possible. LDs were resuspended in 50  $\mu$ L 1X PBS and fixed with an equal volume of 4% paraformaldehyde for 3–4 h. A volume of 8  $\mu$ L LD suspension was deposited onto a parafilm sheet. A formvar/carbon film-coated 100 mesh copper grid (Zhongjingkeyi, China) was put onto the suspension with the film facing down. LDs were allowed to float and adhere to the grid for 2 min. The grid was then washed with a small drop of PB buffer (28 mM NaH<sub>2</sub>PO<sub>4</sub>, 72 mM Na<sub>2</sub>HPO<sub>4</sub>, pH 7.2) for 2 min, three times. The grid was floated on a drop of 20  $\mu$ L PB buffer containing 2% BSA and 0.2% gelatin from cold water fish skin (#G7041, Sigma) to block LDs for 2 min. Next, the grid was incubated with a drop of 8  $\mu$ L rabbit anti-GFP antibody (1:50, #AB6556, Abcam) for 30 min, washed five times with PB buffer (2 min each), incubated with an anti-rabbit IgG-5 nm colloidal gold antibody (1:20, #G7277, Sigma) for 30 min, washed five times with PB buffer (2 min each). After that, the sample grid was re-fixed in 1% glutaraldehyde for 5 min, washed five times with deionized water (2 min each). Uranyl acetate/methyl cellulose solution was prepared by mixing 1 volume of 3% uranyl acetate with 9 volumes of 2% methyl cellulose. A drop of uranyl acetate/methyl cellulose solution was deposited onto a parafilm sheet on ice, and then the sample grid was floated on the drop for 10 min. The grid was carefully removed using a metal loop. Excess liquid was gently removed with a filter paper. The grid was let dry in air for 10 min. The grid was observed and imaged using a transmission electron microscope (Hitachi 7650B) with a Tolara digital camera at 80 kV.

### Measurement of LD membrane fluidity by FRAP

LDs were purified from GFP::DGAT-2 (*hSi56*) or DHS-3::GFP (*ssdSi7*) transgenic lines using a simplified protocol as described above. LD fraction was loaded onto a hemocytometer covered with a coverslip. FRAP was conducted on Zeiss LSM780 equipped with a Plan-Apochromat 100X/NA 1.46 DIC oil objective at room temperature (-22 °C). For FRAP, two GFP::DGAT-2-labeled LDs in the same visual field were chosen. One LD was to be targeted and bleached, and the other for control of non-specific bleaching during image acquisition. A 13  $\times$  13 pixel (0.52  $\mu$ m  $\times$  0.52  $\mu$ m) region of interest (ROI) at the edge of each LD was selected; the ROI of the target LD was photobleached. The bleaching was conducted with a Diode 405-30 mW laser at 100% power output, 20 iterations in 0.57 s. The image acquisition parameters were: excitation wavelength 488 nm with an argon laser, single frame line scan, time-lapse imaging, 5 frames before bleaching and 45 after bleaching, 512  $\times$  512 pixel/frame, pixel dwell time 1.58  $\mu$ s, scan time 0.97 s/frame, scan interval 0 s, averaging number 1, bit depth 12, digital zoom 4x. For data processing, the slope of the decreasing fluorescence of control ROI as a result of non-specific bleaching during imaging was calculated and was used to adjust the fluorescence values of the target ROI. The lowest value of the target ROI immediately after bleaching was identified and was subtracted from all values before and after bleaching. The five values before bleaching were averaged, and the average was revalued as 1; all intensity values were normalized by that value. The average of the last five values usually represents the maximum recovery, which was verified by the appearance of a recovery plateau before the last five. Post-bleaching data were fitted to a natural logarithm function in Microsoft Excel. The frame/time point when fluorescence recovered to half of the maximum recovery was calculated as t-half.

### DMSO supplementation

DMSO (Sigma, #00625) was dissolved in melted NGM at desired concentrations and was poured into 6 cm or 15 cm dishes. Negative control plates were added with equal volumes of water in place of DMSO. OP50 *E. coli* was seeded onto the NGM plates were allowed to grow at room temperature for 2–3 days. Stage L4 animals were inoculated onto the plates to produce progeny. Stage L4 progeny were examined for LD phenotype. For testing the effect of DMSO on LD membrane fluidity, synchronized L1s were inoculated and allowed to grow to 1-day-adult stage, when they were collected for FRAP analysis.

### In vitro fusion assay of artificial LDs

To prepare artificial LDs, 1  $\mu$ mol trioctadecenoin (NU-CHEK, #T-235), 0.25  $\mu$ mol PE(16:0/16:0) (Avanti, #850705 P) and 0.75  $\mu$ mol PC(16:0/18:0) (Avanti, #850456 P) or 0.75  $\mu$ mol PC(16:0/20:4n6) (Santa Cruz Biotechnology, #sc-213759) were mixed in chloroform/methanol (2:1 in volume) in a 1.5 mL microcentrifuge tube, dried under a stream of nitrogen air. The lipid mixture was resuspended in 100  $\mu$ L buffer (150 mM NaCl, 50 mM Tris/HCl, pH 7.5, 1 mM EDTA) and was vortexed for 24 cycles of 10 s on and 10 s off, during which artificial LDs formed and fused. The milky lipid suspension was centrifuged at 20,000  $\times g$  for 5 min. The lower aqueous fraction and pellet were removed. The top fraction was washed twice in 200  $\mu$ L buffer, centrifuged, and lower fraction and pellet were removed. The top LD fraction was resuspended in 50  $\mu$ L buffer, loaded onto a cytometer, and imaged on Nikon ECLIPSE Ni-E wide-field microscope with a Plan-Apo 60X/NA 1.40 oil objective.

### Cell culture

HEK 293 T cells (ATCC) were grown in a 6 cm plate in 5 mL DMEM(H) (Cellmax, #CGM102.05) with 10% fetal bovine serum (Vazyme, #F101-03) in the presence of 1% penicillin/streptomycin (HyClone, #SV30010) at 37 °C and 5% CO<sub>2</sub>. About equal moles of the three plasmids (3  $\mu$ g pEGFP-C1, 3.9  $\mu$ g pFADS2-EGFP, 3.9  $\mu$ g pLPCAT3-EGFP) were transfected with PEI reagent to three plates of HEK293T at -80% confluence. Culture media were refreshed 6 h after transfection, and

cells were allowed to grow and express the proteins for 28 h, when the plate of cells already grew to confluence. Each plate of cells was divided into two halves and plated into two wells laid with cover slips of a 6-well plate. One well was added 2 mL fresh medium with 600  $\mu$ M oleic acid C18:1n9 (Nu-Chek) and 2.5  $\mu$ M red BODIPY-558/568-C12. The other was not added with oleic acid but with equal amount of carrier ethanol. Cells were incubated for 12 h further, then fixed with 4% paraformaldehyde at room temperature for 30 min. Cells attached the coverslips were mounted onto glass slides with antifade mounting medium with DAPI (Beyotime, China) and subjected to confocal imaging. Images were acquired on a Zeiss LSM780 inverted confocal microscope equipped with a Plan-Apochromat 100X/NA 1.46 DIC oil objective in channel mode. GFP and BODIPY were excited with 488 nm and 561 nm lasers, respectively. Cells were randomly sampled and measured in a single blind manner. GFP fluorescence distribution and diameters of red BODIPY-labeled LDs in each cell were measured using the ZEN software. pFADS2-EGFP and pLPCAT3-EGFP plasmids were constructed as follows: FADS2 cDNA was PCR amplified firstly with primer SOZ-813F1/R1 from 1st strand cDNA of HEK293T, then with SOZ-810F1/R1 from product of the first PCR. PCR product was cloned into pEGFP-C1 vector using restriction sites NheI and AgeI to obtain pSOZ-341\_CMVp::FADS2::EGFP. Similarly, LPCAT3 cDNA was PCR amplified firstly with primer SOZ-811F1/R1, then with SOZ-808F1/R1. The PCR product was cloned into pEGFP-C1 using NheI and AgeI to obtain pSOZ-339\_CMVp::LPCAT3::EGFP. The PCR primers were:

SOZ-808F1/R1:  
 ATAAGCTAGC(NheI)GCCACCATGGCGTCCTCAGCG/GGAT  
 ACCGGT(AgeI)TTTCCATCTTCTTAACTTC  
 SOZ-810F1/R1:  
 ATAAGCTAGC(NheI)GCCACCATGGGAAGGGAGGGAA/GGAT  
 ACCGGT(AgeI)TTTTGTGAAGGTAGGCGT  
 SOZ-811F1/R1:  
 ATGGCGTCCTCAGCGGAGGGGACGAGGGGA/TTCCATCTTCTT  
 TAACTTCTCTTCCTTGGCACCA  
 SOZ-813F1/R1:  
 ATGGGGAAGGGAGGGAACCGAGGGCGA/TTTGTGAAGGTAGGC  
 GTCCAGGCCACAGCTTC

## Statistics and reproducibility

Most statistical tests were unpaired two-sample two-tailed *t*-tests conducted with Microsoft Excel software. Most of the experiments were tried two to three times. The data of one trial is presented and is typical of the different trials. No statistical method was used to pre-determine sample size. The allocation and sampling of worm samples and human cell samples were randomized. Some of the fusion-positive animal counting experiments and human cell LD size measurement experiments were conducted in a single or double blind manner. Other experiments were not conducted in a blind manner.

## Reporting summary

Further information on research design is available in the Nature Portfolio Reporting Summary linked to this article.

## Data availability

All study data are included in the article and/or supporting information. Source data is also provided. Source data are provided with this paper.

## References

- White, M. D., Bosio, C. M., Duplantis, B. N. & Nano, F. E. Human body temperature and new approaches to constructing temperature-sensitive bacterial vaccines. *Cell. Mol. Life Sci. CMLS* **68**, 3019–3031 (2011).
- Bartelt, A. & Heeren, J. Adipose tissue browning and metabolic health. *Nat. Rev. Endocrinol.* **10**, 24–36 (2014).
- Ariotti, N. et al. Postlipolytic insulin-dependent remodeling of micro lipid droplets in adipocytes. *Mol. Biol. Cell* **23**, 1826–1837 (2012).
- Paar, M. et al. Remodeling of lipid droplets during lipolysis and growth in adipocytes. *J. Biol. Chem.* **287**, 11164–11173 (2012).
- Walther, T. C. & Farese, R. V. Lipid droplets and cellular lipid metabolism. *Annu. Rev. Biochem.* **81**, 687–714 (2012).
- Qian, K. et al. CLSTN3 $\beta$  enforces adipocyte multilocularity to facilitate lipid utilization. *Nature* **613**, 160–168 (2023).
- Gong, J. et al. Fsp27 promotes lipid droplet growth by lipid exchange and transfer at lipid droplet contact sites. *J. Cell Biol.* **195**, 953–963 (2011).
- Jambunathan, S., Yin, J., Khan, W., Tamori, Y. & Puri, V. FSP27 promotes lipid droplet clustering and then fusion to regulate triglyceride accumulation. *Plos One* **6**, e28614 (2011).
- Lyu, X. et al. A gel-like condensation of Cidec generates lipid-permeable plates for lipid droplet fusion. *Dev. Cell* **56**, 2592–2606 (2021).
- Fei, W. et al. Flld1p, a functional homologue of human seipin, regulates the size of lipid droplets in yeast. *J. Cell Biol.* **180**, 473–482 (2008).
- Szymanski, K. M. et al. The lipodystrophy protein seipin is found at endoplasmic reticulum lipid droplet junctions and is important for droplet morphology. *Proc. Natl. Acad. Sci. USA* **104**, 20890–20895 (2007).
- Krahmer, N. et al. Phosphatidylcholine synthesis for lipid droplet expansion is mediated by localized activation of CTP:phosphocholine cytidylyltransferase. *Cell Metab.* **14**, 504–515 (2011).
- Boström, P. et al. Cytosolic lipid droplets increase in size by microtubule-dependent complex formation. *Arterioscler. Thromb. Vasc. Biol.* **25**, 1945–1951 (2005).
- Fei, W. et al. A role for phosphatidic acid in the formation of “supersized” lipid droplets. *PLoS Genet.* **7**, e1002201 (2011).
- Hishikawa, D. et al. Discovery of a lysophospholipid acyltransferase family essential for membrane asymmetry and diversity. *Proc. Natl. Acad. Sci. USA* **105**, 2830–2835 (2008).
- Zhao, Y. et al. Identification and characterization of a major liver lysophosphatidylcholine acyltransferase. *J. Biol. Chem.* **283**, 8258–8265 (2008).
- Hashidate-Yoshida, T. et al. Fatty acid remodeling by LPCAT3 enriches arachidonate in phospholipid membranes and regulates triglyceride transport. *eLife* **4**, e06328 (2015).
- Rong, X. et al. Lpcat3-dependent production of arachidonoyl phospholipids is a key determinant of triglyceride secretion. *eLife* **4**, e06557 (2015).
- Hishikawa, D., Hashidate, T., Shimizu, T. & Shindou, H. Diversity and function of membrane glycerophospholipids generated by the remodeling pathway in mammalian cells. *J. Lipid Res.* **55**, 799–807 (2014).
- Wilfling, F. et al. Triacylglycerol synthesis enzymes mediate lipid droplet growth by relocating from the ER to lipid droplets. *Dev. Cell* **24**, 384–399 (2013).
- Xu, N. et al. The FATP1-DGAT2 complex facilitates lipid droplet expansion at the ER-lipid droplet interface. *J. Cell Biol.* **198**, 895–911 (2012).
- Zhang, S. O. et al. Genetic and dietary regulation of lipid droplet expansion in *Caenorhabditis elegans*. *Proc. Natl. Acad. Sci. USA* **107**, 4640–4645 (2010).
- Zhang, S. O., Trimble, R., Guo, F. & Mak, H. Y. Lipid droplets as ubiquitous fat storage organelles in *C. elegans*. *BMC Cell Biol.* **11**, 96 (2010).
- Li, S. et al. A genetic screen for mutants with supersized lipid droplets in *Caenorhabditis elegans*. *G3* **6**, 2407–2419 (2016).
- Li, S. et al. Specific regulation of thermosensitive lipid droplet fusion by a nuclear hormone receptor pathway. *Proc. Natl. Acad. Sci. USA* **114**, 8841–8846 (2017).

26. Li, A. et al. Bietti crystalline corneoretinal dystrophy is caused by mutations in the novel gene CYP4V2. *Am. J. Hum. Genet.* **74**, 817–826 (2004).

27. Watts, J. L. & Browne, J. Genetic dissection of polyunsaturated fatty acid synthesis in *Caenorhabditis elegans*. *Proc. Natl. Acad. Sci. USA* **99**, 5854–5859 (2002).

28. Beaudoin, F. et al. Heterologous reconstitution in yeast of the polyunsaturated fatty acid biosynthetic pathway. *Proc. Natl. Acad. Sci. USA* **97**, 6421–6426 (2000).

29. Kniazeva, M. et al. Suppression of the ELO-2 FA elongation activity results in alterations of the fatty acid composition and multiple physiological defects, including abnormal ultradian rhythms, in *Caenorhabditis elegans*. *Genetics* **163**, 159–169 (2003).

30. Watts, J. L. Using *Caenorhabditis elegans* to uncover conserved functions of omega-3 and omega-6 fatty acids. *J. Clin. Med.* **5**, 19 (2016).

31. Svensk, E. et al. PAQR-2 regulates fatty acid desaturation during cold adaptation in *C. elegans*. *PLoS Genet.* **9**, e1003801 (2013).

32. Lee, H. C. et al. *Caenorhabditis elegans* mbo-7, a member of the MBOAT family, is required for selective incorporation of polyunsaturated fatty acids into phosphatidylinositol. *Mol. Biol. Cell* **19**, 1174–1184 (2008).

33. Matsuda, S. et al. Member of the membrane-bound O-acyltransferase (MBOAT) family encodes a lysophospholipid acyltransferase with broad substrate specificity. *Genes Cells* **13**, 879–888 (2008).

34. Lyman, G. H., Preisler, H. D. & Papahadjopoulos, D. Membrane action of DMSO and other chemical inducers of Friend leukaemic cell differentiation. *Nature* **262**, 361–363 (1976).

35. Liu, Y. N. et al. Membrane fluidity is involved in the regulation of heat stress induced secondary metabolism in *Ganoderma lucidum*. *Environ. Microbiol.* **19**, 1653–1668 (2017).

36. Ma, D. K. et al. Acyl-CoA dehydrogenase drives heat adaptation by sequestering fatty acids. *Cell* **161**, 1152–1163 (2015).

37. Gao, C. et al. Endocrine pheromones couple fat rationing to dauer diapause through HNF4α nuclear receptors. *Sci. China Life Sci.* **64**, 2153–2174 (2021).

38. Harayama, T. & Shimizu, T. Roles of polyunsaturated fatty acids, from mediators to membranes. *J. lipid Res.* **61**, 1150–1160 (2020).

39. Tauchi-Sato, K., Ozeki, S., Houjou, T., Taguchi, R. & Fujimoto, T. The surface of lipid droplets is a phospholipid monolayer with a unique fatty acid composition. *J. Biol. Chem.* **277**, 44507–44512 (2002).

40. Bartz, R. et al. Lipidomics reveals that adiposomes store ether lipids and mediate phospholipid traffic. *J. Lipid Res.* **48**, 837–847 (2007).

41. Arisawa, K., Ichi, I., Yasukawa, Y., Sone, Y. & Fujiwara, Y. Changes in the phospholipid fatty acid composition of the lipid droplet during the differentiation of 3T3-L1 adipocytes. *J. Biochem.* **154**, 281–289 (2013).

42. Arisawa, K. et al. Saturated fatty acid in the phospholipid monolayer contributes to the formation of large lipid droplets. *Biochem Biophys. Res Commun.* **480**, 641–647 (2016).

43. Puri, V. et al. Fat-specific protein 27, a novel lipid droplet protein that enhances triglyceride storage. *J. Biol. Chem.* **282**, 34213–34218 (2007).

44. Chung, J. et al. LDAF1 and Seipin form a lipid droplet assembly complex. *Dev. Cell* **51**, 551–563.e557 (2019).

45. Pagac, M. et al. SEIPIN regulates lipid droplet expansion and adipocyte development by modulating the activity of glycerol-3-phosphate acyltransferase. *Cell Rep.* **17**, 1546–1559 (2016).

46. Romanauska, A. & Köhler, A. The inner nuclear membrane is a metabolically active territory that generates nuclear lipid droplets. *Cell* **174**, 700–715.e718 (2018).

47. Ding, L. et al. Seipin regulates lipid homeostasis by ensuring calcium-dependent mitochondrial metabolism. *EMBO J.* **37**, e97572 (2018).

48. Pinot, M. et al. Lipid cell biology. Polyunsaturated phospholipids facilitate membrane deformation and fission by endocytic proteins. *Science* **345**, 693–697 (2014).

49. Saito, H. et al. Coalescence of lipid emulsions in floating and freeze-thawing processes: examination of the coalescence transition state theory. *J. Colloid Interface Sci.* **219**, 129–134 (1999).

50. Rong, X. et al. LXR<sub>Rs</sub> regulate ER stress and inflammation through dynamic modulation of membrane phospholipid composition. *Cell Metab.* **18**, 685–697 (2013).

51. Moessinger, C. et al. Two different pathways of phosphatidylcholine synthesis, the Kennedy Pathway and the Lands Cycle, differentially regulate cellular triacylglycerol storage. *BMC Cell Biol.* **15**, 43 (2014).

52. Zhang, P. et al. Proteomic study and marker protein identification of *Caenorhabditis elegans* lipid droplets. *Mol. Cell. Proteom.: MCP* **11**, 317–328 (2012).

53. Bai, Y. et al. X-ray structure of a mammalian stearoyl-CoA desaturase. *Nature* **524**, 252–256 (2015).

54. Kory, N., Farese, R. V. Jr. & Walther, T. C. Targeting fat: mechanisms of protein localization to lipid droplets. *Trends Cell Biol.* **26**, 535–546 (2016).

55. Mahanti, P. et al. Comparative metabolomics reveals endogenous ligands of DAF-12, a nuclear hormone receptor, regulating *C. elegans* development and lifespan. *Cell Metab.* **19**, 73–83 (2014).

56. Nakano, M., Kelly, E. J., Wiek, C., Hanenberg, H. & Rettie, A. E. CYP4V2 in Bietti's crystalline dystrophy: ocular localization, metabolism of ω-3-polyunsaturated fatty acids, and functional deficit of the p.H331P variant. *Mol. Pharmacol.* **82**, 679–686 (2012).

57. Hata, M. et al. Reduction of lipid accumulation rescues Bietti's crystalline dystrophy phenotypes. *Proc. Natl. Acad. Sci. USA* **115**, 3936–3941 (2018).

58. Lockhart, C. M., Nakano, M., Rettie, A. E. & Kelly, E. J. Generation and characterization of a murine model of Bietti crystalline dystrophy. *Investig. Ophthalmol. Vis. Sci.* **55**, 5572–5581 (2014).

59. Gao, P. et al. Accumulation of lipid droplets in a novel Bietti crystalline dystrophy zebrafish model with impaired PPAR $\alpha$  pathway. *Investig. Ophthalmol. Vis. Sci.* **63**, 32 (2022).

60. Jia, R. et al. AAV-mediated gene-replacement therapy restores viability of BCD patient iPSC derived RPE cells and vision of Cyp4v3 knockout mice. *Hum. Mol. Genet.* **32**, 122–138 (2023).

## Acknowledgements

We thank our lab members and Dr. Xiao Liu for technical help and discussion, Drs. Weiwei Zhang, Hailong Wang, and Shi Xu for help on cell culture, cell lines and GC experiments, Dr. Ye Tian for antibody, Mr. Xin Xu, Drs. Ligong Chen, Ying Li, Xiaomin Li, Xin Liang, and Yiguo Wang of Tsinghua Univ. for technical and logistic support on TEM and protein gels, and staff at LipidALL Technologies for lipidomics support. Some of the nematode strains were obtained from the *Caenorhabditis* Genetics Center of USA and Mitani Lab through the National Bio-Resource Project of the MEXT of Japan. This work was supported by National Natural Science Foundation of China Grants 91857106 & 32171169 to S.O.Z. Q.L. was partly supported by Beijing Postdoctoral Research Foundation.

## Author contributions

Q.L., C.Z., and S.O.Z. designed research; Q.L., Xiaofang Z., X.Z., C.Z., and S.O.Z. performed research and analyzed data; and Q.L. and S.O.Z. wrote the paper.

## Competing interests

The authors declare no competing interests.

## Additional information

**Supplementary information** The online version contains supplementary material available at <https://doi.org/10.1038/s41467-025-59256-6>.

**Correspondence** and requests for materials should be addressed to Shaobing O. Zhang.

**Peer review information** *Nature Communications* thanks Xuchao Lyu and the other anonymous reviewer(s) for their contribution to the peer review of this work. A peer review file is available.

**Reprints and permissions information** is available at <http://www.nature.com/reprints>

**Publisher's note** Springer Nature remains neutral with regard to jurisdictional claims in published maps and institutional affiliations.

**Open Access** This article is licensed under a Creative Commons Attribution-NonCommercial-NoDerivatives 4.0 International License, which permits any non-commercial use, sharing, distribution and reproduction in any medium or format, as long as you give appropriate credit to the original author(s) and the source, provide a link to the Creative Commons licence, and indicate if you modified the licensed material. You do not have permission under this licence to share adapted material derived from this article or parts of it. The images or other third party material in this article are included in the article's Creative Commons licence, unless indicated otherwise in a credit line to the material. If material is not included in the article's Creative Commons licence and your intended use is not permitted by statutory regulation or exceeds the permitted use, you will need to obtain permission directly from the copyright holder. To view a copy of this licence, visit <http://creativecommons.org/licenses/by-nc-nd/4.0/>.

© The Author(s) 2025